Ceramics International 47 (2021) 23725–23748

Contents lists available at ScienceDirect

Ceramics International

journal homepage: www.elsevier.com/locate/ceramint

Review article

Recent progress in barium zirconate proton conductors for electrochemical hydrogen device applications: A review

M. Khalid Hossain [a,b,*], Rajesh Chanda [c], A. El-Denglawey [d], Tanvir Emrose [e], M. Tayebur Rahman [f], Manik C. Biswas [g], Kenichi Hashizume [a]

[a] Department of Advanced Energy Engineering Science, Interdisciplinary Graduate School of Engineering Science, Kyushu University, Fukuoka 816-8580, Japan
[b] Atomic Energy Research Establishment, Bangladesh Atomic Energy Commission, Dhaka, 1349, Bangladesh
[c] Department of Chemical Engineering, Jashore University of Science and Technology, Jashore, 7408, Bangladesh
[d] Department of Physics, College of University College at Turabah, Taif University, PO Box 11099, Taif 21944, Saudi Arabia
[e] School of Electrical Engineering and Computer Science, Louisiana State University, Baton Rouge, LA 70803, USA
[f] Department of Materials Science and Engineering, University of Rajshahi, Rajshahi 6205, Bangladesh
[g] North Carolina State University, Raleigh, NC, 27606, USA

ARTICLE INFO

Keywords:
Barium zirconate ($BaZrO_3$)
Proton-conducting oxide
Hydrogen pump
Hydrogen sensor
Fuel cell electrolyte
Proton conductivity
Energy materials

ABSTRACT

Electrochemical hydrogen devices like fuel cells are widely investigated as promising technologies to mitigate the rising environmental challenges and enhance the renewable energy economy. In these devices, proton-conducting oxides (PCOs) are applied as electrolyte materials to transport protons. Excellent physical stability and higher proton transport number are two essential properties of electrolyte materials. Doped $BaZrO_3$ (BZO) is a solid ion-conducting perovskite material with high chemical stability and good proton-conducting properties at an intermediate temperature range of 400–650 °C. Therefore, BZO is an attractive material among the exciting proton-conducting oxides as electrolyte material. To enhance the proton transport properties and improve the material fabrication process of BZO, techniques such as the use of dopants, sintering aid, synthesis methods are crucial. The present review work highlights the applications of BZO as electrolyte material in electrochemical hydrogen devices such as hydrogen isotopes separation systems, hydrogen sensors, hydrogen pumps, and protonic ceramic fuel cells (PCFCs) or solid oxide fuel cells (SOFCs). The central section of this review summarizes the recent research investigations of these applications and provides a comprehensive insight into the various synthesis process, doping, sintering aid, operating environments, and operating condition's impact on the composition, morphology, and performance of BZO electrolyte materials. Based on the reviewed literature, remarks on current challenges and prospects are provided. The presented information on in-depth analysis of the physical properties of barium zirconate electrolyte's along with output performance will guide aspirants in conducting research further on this field.

1. Introduction

The ever-increasing energy demand and depletion of non-renewable energy resources have been the center stage of innovation. Among the various technological devices to confront these challenges, electrochemical hydrogen devices are being thoroughly researched for energy conversion and gas separation processes [1,2]. Among the applications, PCFCs are used in the sector of sustainable energy conversion, whereas hydrogen pump is used in the separation of hydrogen from steam reforming or in the ammonia synthesis process [3–7]. The performance of these devices is highly dependent on electrolyte materials development [2]. Therefore, the research efforts are focused on the exploration of the appropriate materials, their synthesis, and performance evaluation at the desired operational window.

Proton-conducting oxide (PCO) materials due to their low cost and high proton conduction property, are desirable materials for electrochemical devices. The proton conduction in oxide materials such as $BaTiO_3$, ZnO was discovered in the 1950s [8,9]. However, the pioneering work of Iwahara and coworkers in the 1980s has demonstrated the practical application of PCO materials as proton conductors in oxide materials with both experimental and theoretical investigation [10,11].

* Corresponding author. Department of Advanced Energy Engineering Science, Interdisciplinary Graduate School of Engineering Science, Kyushu University, Fukuoka 816-8580, Japan.
E-mail addresses: khalid.baec@gmail.com, khalid@kyudai.jp (M.K. Hossain).

https://doi.org/10.1016/j.ceramint.2021.05.167
Received 3 April 2021; Received in revised form 14 May 2021; Accepted 18 May 2021
Available online 26 May 2021

List of abbreviations

BCO	$BaCeO_3$
BZO	$BaZrO_3$
BZY	Y-doped barium zirconate
BZY10	$BaZr_{0.9}Y_{0.1}O_{3-\delta}$
BZYC	$BaZr_{0.955}Y_{0.03}Co_{0.015}O_{3-\delta}$
CEM	Chudley–Elliot model
E_a	Activation energy
EIS	Electrochemical impedance spectroscopy
EMF	Electromotive force
GB	Grain boundary
HRM	Hall and Ross Model
H–SOFC	Proton-conducting solid oxide fuel cells
IT-SOFC	Intermediate temperature solid oxide fuel cell
OCV	Open-circuit voltage
PCFC	Protonic ceramic fuel cells
PCO	Proton-conducting oxide
P_{max}	Peak power density
SEM	Scanning electron microscope
R_p	Polarization resistance
R_Ω	Ohmic resistance
SOFC	Solid oxide fuel cell
SSM	Singwi and Sjölander Model
SSRS	Solid-state reactive sintering
XRD	X-ray diffraction

In PCO materials, the proton transport is driven by the protonic defects that are created due to the interaction of the lattice structure of materials with hydrogen-water-containing gas components at moderate temperatures [12]. Kreuer et al. explained the relations of structural and chemical parameters on the defect chemistry and transport properties in PCO materials, particularly proton transport in cerates and zirconates of alkaline-earth elements at wet conditions [12,13].

The application of PCO materials as hydrogen transport in devices such as electrolyte material for solid oxide fuel cell (SOFC) depends primarily on two aspects: (1) the temperature of proton transport and (ii) material properties such as thermal and chemical stability. The initial promising materials, such as yttria-stabilized zirconia (oxide ion conductors) operate better at a high-temperature range of 650–800 °C [12]. To overcome the high operating temperature hindrance, PCO materials are investigated for proton conduction application at a temperature range of 400–650 °C [14], and due to the lower activation energy (E_a), PCO materials showed excellent performance at 400–650 °C temperature zone [15]. Among the studied PCOs, $BaCeO_3$ and $BaZrO_3$ are the most promising oxides for such applications. $BaCeO_3$ has high proton conductivity for the application of proton ceramic oxides. However, in a CO_2-present environment, it reacts with CO_2 wherein the presence of water, decomposes into CeO_2 and $Ba(OH)_2$ at operating temperature [16,17]. In this respect, $BaZrO_3$ (BZO) has superior material stability in the presence of CO_2 and water; however, it has lower proton conductivity compare to barium cerates. Therefore, many investigations are carried out to improve the proton conductivity and easy processing of BZO material.

Doping with trivalent cations such as Y^{3+}, In^{3+}, Yb^{3+}, Gd^{3+}, etc. is the most used technique to improve the proton conductivity of BZO material [18,19]. Among the doped BZO, yttrium doped BZO shows superior proton conductivity and better chemical, mechanical stability [20]. Consequently, investigations by varying the concentration of doping, synthesis techniques are applied to fabricate high-performing doped BZO material [21]. In addition, the sinterability of doped BZO has remained a key stumbling block for large-scale production although being a promising oxide material. Different sintering aids like ZnO, CuO, NiO were incorporated into the doped BZO to lower the required sintering temperature [20,22,23].

The growing number of research works on the variation of important fabrication parameters and their impact on the intrinsic structure-property relationship of BZO material [24,25] is a demanding task for an aspiring researcher to follow. Therefore, in this review, the most recent developments of BZO as materials for application in electrochemical devices are summarized and presented. In the first section of the review, short overviews of BZO materials, hydrogen pumps, hydrogen sensors, and PCFCs are given to help to understand the basic phenomena of each topic. In the following section, BZO material as an electrolyte in the application of hydrogen pumps, hydrogen sensors, and solid oxide fuel cell devices is presented. An intensive focus is given to the doping, sintering aid, synthesis methods, operating conditions, operation environment's influence on the final grain size, activation energy, total conductivity, and peak power density (P_{max}) of BZO as electrolytes in the fuel cell. Based on the reviewed literature, remarks on current challenges and prospects are provided (Fig. 1).

2. Proton conductors

Proton conductors are functional materials through which positively charged protonic species, for example, H^+, H_3O^+, and even NH_4^+ ions are considered to migrate. Generally, protonic conduction declines at higher temperatures due to reversible or irreversible loss of carriers such as water molecules in polymers, melting or decomposition of acid salts or hydrates hydroxides, and reversible loss of protons (water molecule) from oxide materials. Thus, comparatively narrow temperature ranges are suitable for functioning proton conductors. However, it depends on the types of proton conductors, and their operating temperatures, the conductivity of protonic conductors can be achieved at the range of 10^{-1} - 10^{-5} S/cm [26].

Proton conductors can be used in various electrochemical devices such as hydrogen sensors [27–34], humidity sensors [32], hydrogen pumps [35–41], hydrogen gas separation systems [2,37,42–53], the membrane of water electrolyzers [54–57], batteries [58–62], and electrolytes of fuel cells [63–69]. There are different types of proton conductors including organic polymers [70], inorganic oxides [71], β-alumina oxides [72], lattice defect oxides [73], etc. Among all types of proton conductors, only lattice defect oxides i.e., perovskite proton conductors can be used at a high temperature of 200 °C or higher because other types of proton conductors lose their proton conductivity due to dehydration or decomposition when the temperature is raised.

Based on available proton concentrations and mobilities data, proton conductivity has been calculated for elevated temperature range and represented in Fig. 2 [12]. Maximum proton conductivity is found in perovskite-type oxides, such as $BaZrO_3$, $BaCeO_3$, $BaTbO_3$, and $BaThO_3$ (Fig. 2) due to having extensive negative enthalpies for hydration and less activation energies for the migration of protons [74]. Therefore, lattice defect type oxides attracted the attention of scientists and researchers that can be used for SOFC solid electrolytes, and other electrochemical devices operated at high temperatures ranging from 600 °C to 1000 °C.

3. Perovskite $BaZrO_3$ proton conductor

Barium zirconate ($BaZrO_3$) is a well-known perovskite material, widely studied/applied in electronic and refractory sectors. This material possesses high melting temperature (3193 K), low thermal conductivity, low dielectric loss, a resistant owing to insignificant thermal expansion coefficient ($\alpha = 32 \times 10\ K^{-9}$ at the range of 298 K and 1353 K), and excellent mechanical and structural properties at elevated

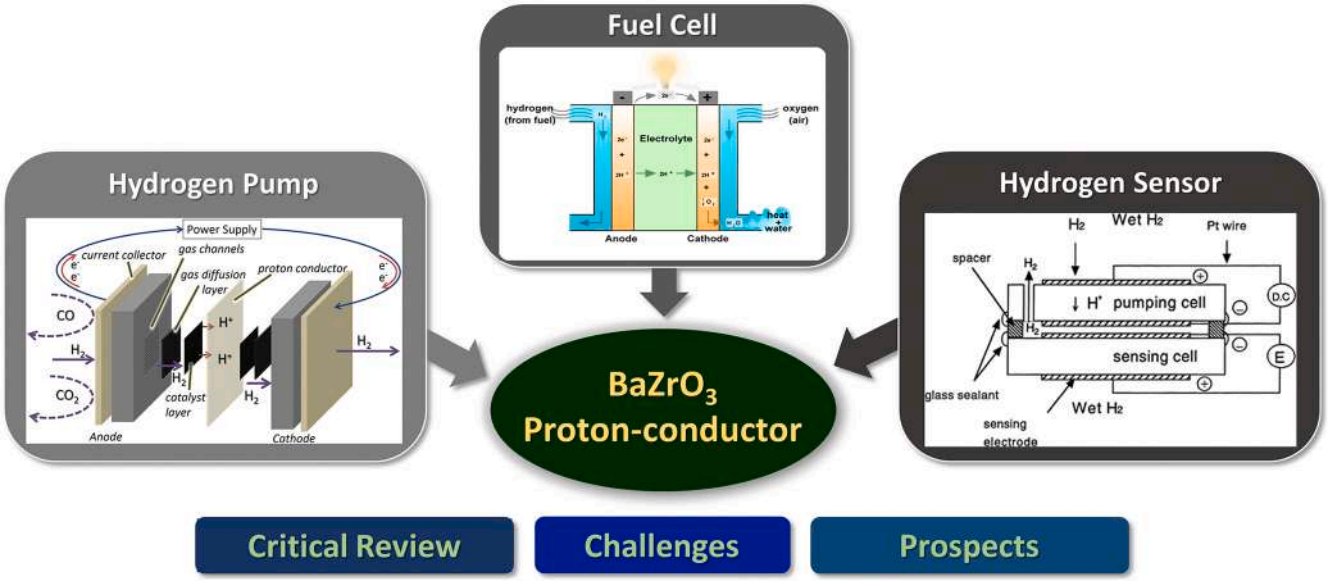

Fig. 1. Schematic representation showing an overview of the major contents of this review article.

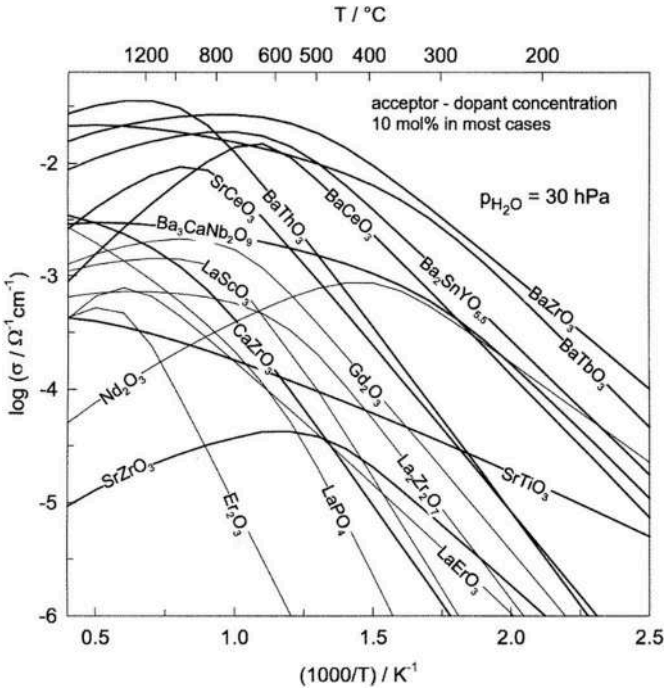

Fig. 2. Construction of proton conductivity graph for various oxides based on available proton concentrations and mobilities data. Bold lines refer to the conductivity of perovskite-type oxides [12].

temperature [75]. There is no phase change occurs at temperature ranges from 4 K to 1600 K that makes it a suitable candidate to use as a structural material, thermal barrier coating [75], thin-film deposition substrate, dielectric materials, fuel cell electrolytes, hydrogen separation membranes, etc. [76–78].

Ideal perovskite oxides have general chemical formula ABO_3, where both A and B site is occupied by cations and O site by anions and constructed a face-centered cubic (fcc) lattice structure. The desirable properties can be induced in perovskite oxides simply by substituting or partially substituting the atoms situated at A or B position [79]. $BaCeO_3$ and $BaZrO_3$ materials are the best proton conductor compared with other perovskite oxides [12] (Fig. 2). Among all types of $BaZrO_3$, Y-doped $BaZrO_3$ ($BaZr_{1-x}Y_xO_{3-\delta}$) exhibits high proton conductivity and excellent stability at elevated temperatures. According to Fig. 3 it is seen that oxygen vacancies are created when two Zr^{4+} are replaced by two Y^{3+}. The generated oxygen vacancies can absorb water molecules leading to produce protonic defects in the crystal structure, resulting in increased proton transport phenomenon.

However, the presence of an excess amount of Zr makes $BaZrO_3$ perovskite highly refractive and contains grain boundaries with enormous resistivity. Therefore, to fabricate dense membranes and grain growth, this material needs to be sintered at a very high temperature, generally between 1600 °C and 1700 °C for a prolonged time (>24 h). The prolonged sintering at a higher temperature may reduce total proton conductivity in $BaZrO_3$ due to alteration of true compositional stoichiometry for partial losses of Ba by evaporation, leading to segregation of yttrium oxide (Y_2O_3) from the bulk phase [81].

4. Electrochemical hydrogen devices

The basic electrochemical hydrogen devices can be constructed as, *Electrode (anode)/Proton conducting solid (Electrolyte)/Electrode (cathode)* [82]. Recently, proton (H^+) conducting electrolytes have been using extensively in electrochemical devices. This becomes possible as a proton has a small radius, which helps it to fit into the layered structure of the cathode [82]. In electrochemical hydrogen devices, two fundamental functions of proton-conducting oxides can be utilized. One of them is electromotive force (EMF), and another is electrochemical hydrogen transportation through the solids.

In the proton-conducting electrolyte of an electrochemical hydrogen

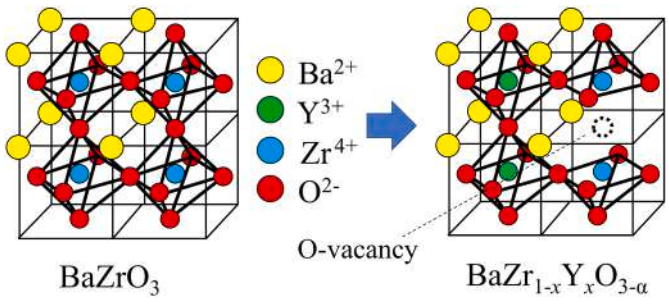

Fig. 3. Formation of oxygen vacancies in Y-doped $BaZrO_3$ [80].

device, an electromotive force (EMF) is utilized by following the same principle of a galvanic cell, where a solid material is used as an electrolyte. When the EMF is used in a device to generate signals, the device is called a hydrogen activity sensor. On the other hand, when the EMF is used to produce electricity, the device is termed a fuel cell. Electrochemical transportation of hydrogen is an important function of a protonic conductor, which is possible due to the preferred proton migration through the solid electrolyte materials. The device that follows the principle to separate hydrogen or extract hydrogen from the gas mixture is named hydrogen pump.

4.1. Hydrogen sensors

In respect of combustion characteristics, hydrogen (H_2) has the lowest inflaming energy (0.017 mJ), wide combustible range (4–75%), high heat of combustion (142 kJ/g H_2), detonation sensitivity, high flaming velocity, and ignition temperature (560 °C). Hydrogen has no color, odor, and taste; thus, it is almost impossible to detect by human senses. However, due to high flammability, strong reducing properties, and permeability through various materials, rapid and accurate detection of this gaseous element is essential in several applications to prevent the risk of an explosion and damages [83]. A hydrogen sensor is a transducer device that is used to detect the presence of hydrogen gas molecules in the range of parts per million (ppm) to levels near the lower explosive limit (4% H_2 in the air), and to concentrations near 100%. At present electrochemical, thermoelectric, semiconductor, metallic, optical, and acoustic ones, etc. hydrogen sensors are available for commercial uses [83]. The basic construction of a hydrogen sensor is represented in Fig. 4(a) as well as the limiting-current-type hydrogen sensor in Fig. 4(b). Interaction of hydrogen molecules with the sensing material of the sensor can cause fluctuations in mechanical properties, electrical properties, temperature, mass, and even in refractive index resulting in an electrical impulse amplified proportionally to the gas concentration for practical applications.

This device became affordable, portable, and in situ hydrogen concentration detection in several applications due to its miniature size and low cost. Nowadays, this device has been using reliably in diverse hydrogen dominating applications, for example, fuel cell, purification, and storage of hydrogen, safety monitoring of hydrogen production plants, storage tanks, pipelines, refueling stations, and automotive vehicles [83].

4.2. Hydrogen pumps

Hydrogen is an important energy carrier material to solve several environmental issues like toxic emissions, carbon-free sustainability, and alternative energy source. This material has also been extensively used in many sectors, including chemical, metallurgical, petrochemical industries as raw material. So far, hydrogen has mostly been sourced from the reformation of fossil fuels containing other gases, such as CH_4, H_2S, CO, and CO_2 [84]. Therefore, producing hydrogen with high purity demands an efficient separation and purification to be used in diverse applications suitably.

Several technologies have been followed to produce hydrogen, for example, cryogenic distillation, pressure swing adsorption galvanic hydrogen pumps as well as non-galvanic hydrogen separation pumps. Fig. 5 illustrates the construction and working principle of an electrochemical hydrogen separation pump. In this system, proton-conducting $BaZrO_3$ perovskite oxide material is used as an electrolyte layer. Proton is generated at the anode by following the chemical reaction mentioned in Eq. (1) when direct current is applied to the cell. This produced proton diffuses through the electrolyte layer towards the cathode and forms hydrogen through recombination by the following Eq. (2).

$$\text{Anode: } H_2 \rightarrow 2H^+ + 2e^- \quad (1)$$

$$\text{Cathode: } 2H^+ + 2e^- \rightarrow H_2 \quad (2)$$

Thus, according to this method, hydrogen can be separated in a controlled way by merely regulating the applied current of the electrochemical cell. However, the hydrogen pumping is also influenced by several operating factors such as temperature, partial pressures of hydrogen, and water vapor in the mixture [84].

4.3. Fuel cells

A basic fuel cell converts the chemical energy of a fuel directly into electricity without any combustion and emission. It is constructed with a cathode, ion-conducting electrolyte layer, and an anode (Fig. 6). In a fuel cell, a fuel like hydrogen is supplied from an anode, and an oxidant, usually oxygen is supplied from the cathode where electrolyte prevents the direct combustion of the fuel (H_2) and oxidant (O_2). This electrolyte layer restricts the gases to diffuse, however, it allows ions to transfer through it [85].

Solid oxide fuel cells can be classified into three categories (Fig. 6), such as oxygen ion transfer type, hydrogen ion transfer type, and mixed ion transfer type. In an oxygen ion transfer type fuel cell, electricity is produced when oxygen ion passes through the electrolyte membrane and reacts with hydrogen at the anode, releasing water as a byproduct (Fig. 6(a)). Electricity is generated between the electrodes due to the formation of discharged electrons in the water production process. The anodic and cathodic reactions are as follows:

$$\text{Anode: } H_2 + O^{2-} \rightarrow H_2O + 2e^- \quad (3)$$

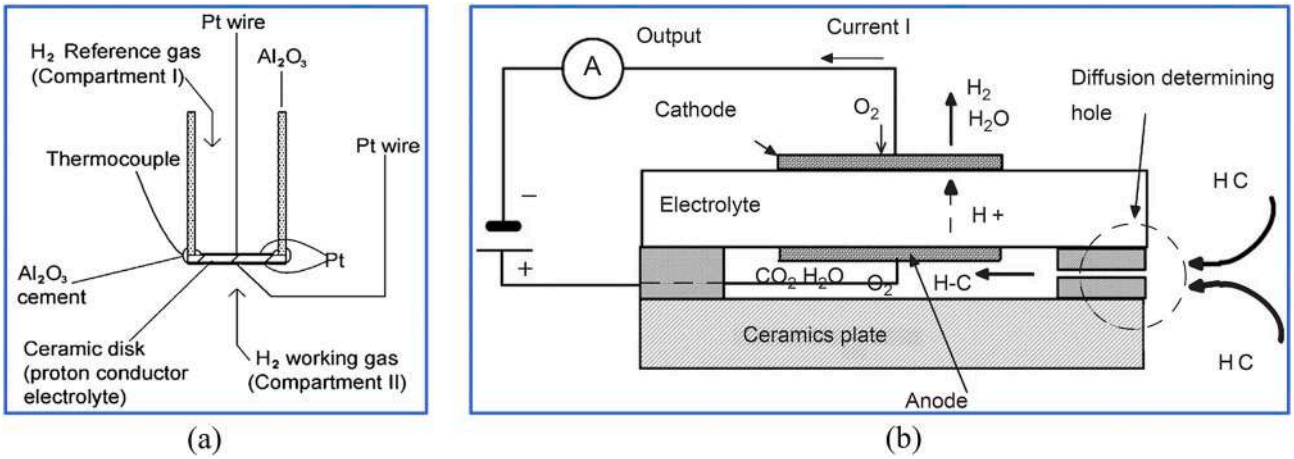

Fig. 4. Basic diagram of (a) a simple hydrogen sensor [18], and (b) limiting-current-type hydrogen sensor [33].

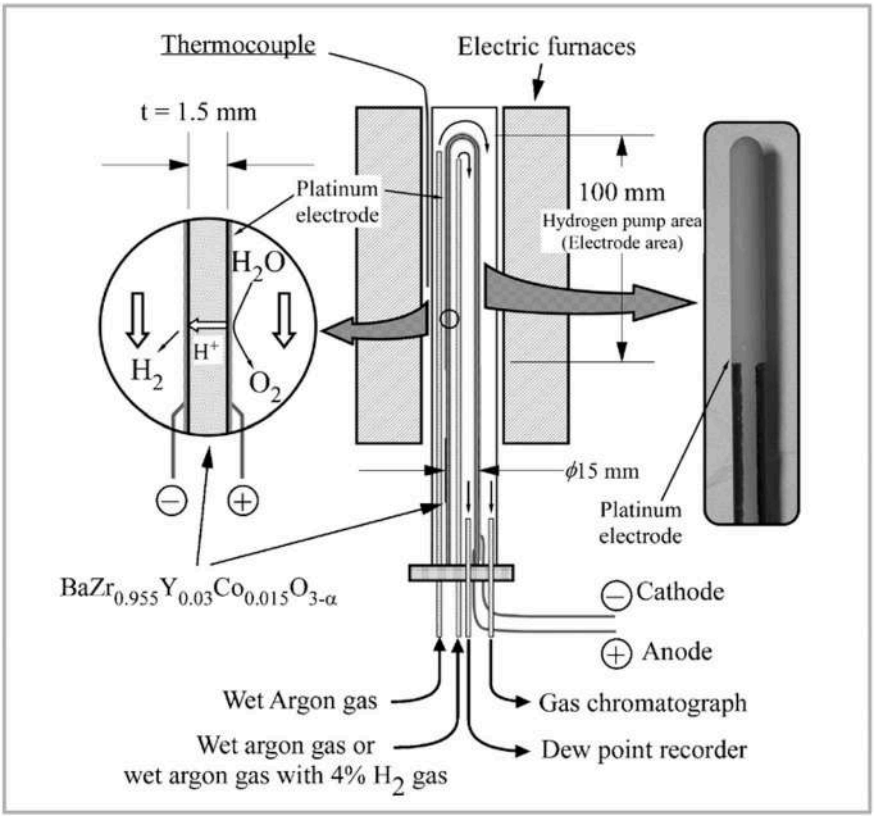

Fig. 5. Construction of a hydrogen pump device as well as a photo of a proton conductor [19].

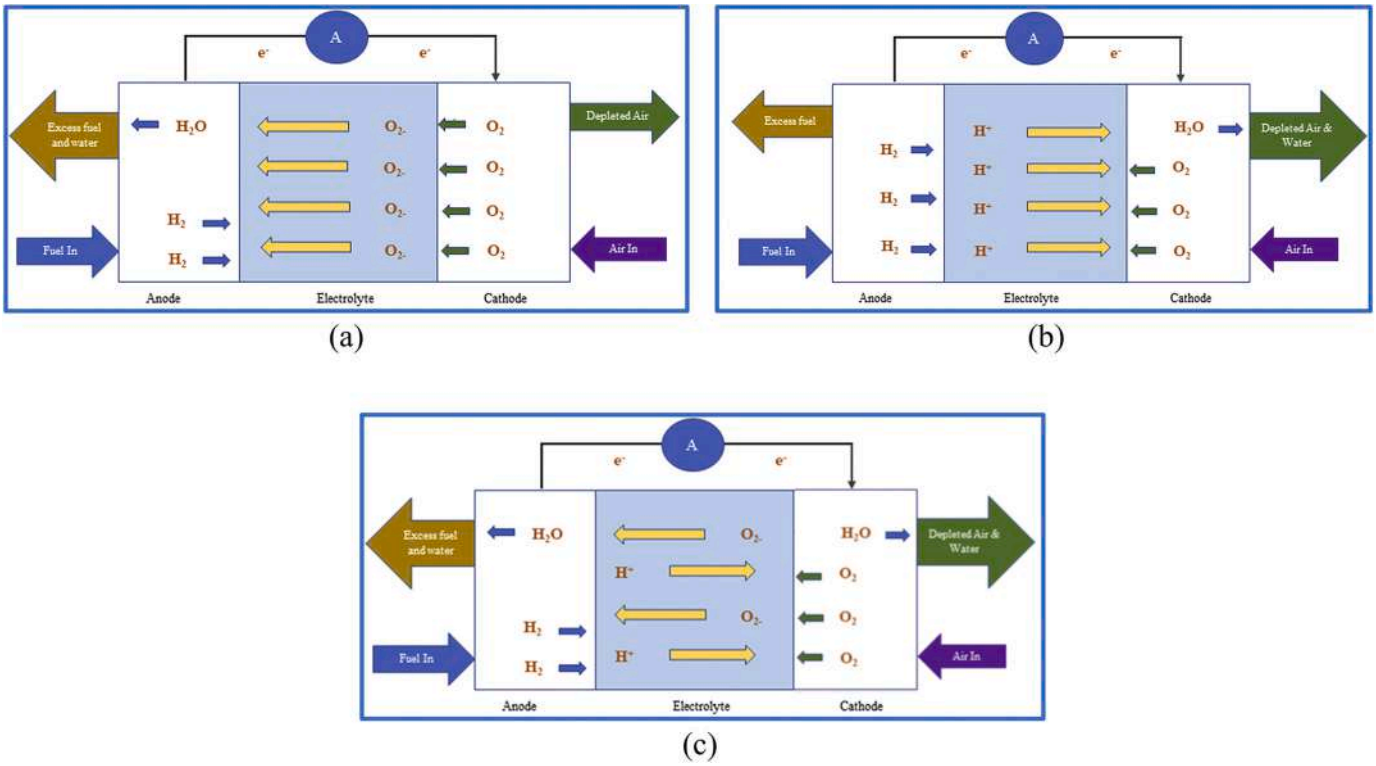

Fig. 6. Operating principle of (a) oxygen ion transfer, (b) hydrogen ion transfer, and (c) mixed ion transfer type solid oxide fuel cells [86].

Cathode: $O_2 + 4e^- \rightarrow 2O^{2-}$ (4)

In a hydrogen ion conduction type fuel cell, water is formed at the cathode; thus, electricity is generated as a result of passing hydrogen ions across the electrolyte (Fig. 6 (b)). The anodic and cathodic reactions are as follows:

Anode: $H_2 \rightarrow 2H^+ + 2e^-$ (5)

Cathode: $4H^+ + O_2 + 4e^- \rightarrow 2H_2O$ (6)

In a mixed ion full cell, electricity is produced when both oxygen and hydrogen migrate through the electrolytic layer towards anode and cathode, respectively (Fig. 6 (c)).

In fuel cells, usually hydrogen, methanol, ethanol, and other alcohols are used as fuel to produce electrical energy. The operating temperature depends on the type of electrolyte used in this cell. Generally, fuel cells based on polymers can be operated at low temperatures (~80 °C) and cells based on solid oxide, for example, gadolinium doped ceria and yttrium stabilized zirconia at intermediate temperature (~ 650 °C or below) [85]. Based on operating temperature, fuel cells can be classified as polymer electrolyte membrane (70–110 °C), alkali fuel cell (100–250 °C), phosphoric acid fuel cell (150–250 °C), molten carbonate fuel cell (500–700 °C) and solid oxide fuel cell (700–1000 °C). In comparison with other fuel cells, solid oxide fuel cell is very popular for high efficiency, both electricity and heat generation, and good fuel flexibility as various hydrocarbon fuels can be used. Besides, this type of fuel cell shows excellent reliability during long-term continuous operation in high temperature and less expensive as no need to use noble metal catalysts.

5. Review on recent literature

Recent progress on the barium zirconate electrolyte-based electrochemical hydrogen devices like hydrogen sensors, hydrogen pumps, and fuel cells, their preparation techniques, and performances are discussed in the following sections.

5.1. Hydrogen sensors and hydrogen pumps

Doped $BaZrO_3$ materials, due to their high proton conductivity and chemical stability at solid oxide fuel cell operating temperatures of 400–700 °C have been studied as solid electrolytes in hydrogen pump [87] and hydrogen sensor applications [33,34]. Among a group of doped perovskite oxides, Schneller and Schober, T. (2003) [34] studied the fabrication process of proton-conducting $BaZr_{0.80}Y_{0.20}O_{3-x}$ films which can be applied to the sensor devices like hydrogen sensors. The study investigated the chemical deposition solution technique, which is very cost-effective and has an easy fabrication process and low operating temperature. The solution produced by this method was found to be very stable for more than six months. From the X-ray diffraction (XRD) pattern and scanning electron microscope (SEM) image analysis, the authors concluded that hydrogen sensors based on this film are very responsive because of its thin structure. Borland et al. have studied $BaZr_{0.9}Y_{0.1}O_{3-\delta}$ (BZY10) and $BaCe_{0.6}Zr_{0.3}Y_{0.1}O_{3-\delta}$ prepared by the SSR route as solid electrolyte in potential hydrogen sensor for tritium detection in fusion reactors [18]. As a potential hydrogen sensor, Taniguchi et al. have studied $BaZr_{0.4}Ce_{0.4}In_{0.2}O_3$ proton-conducting ceramic properties by EMF responses of a hydrogen concentration cell and an electrochemical hydrogen permeation test [33]. For the study, a 0.45 mm thick electrolyte ceramic material, prepared using the SSR route, and platinum paste was used as an electrode. The current-potential characteristics under pure H_2 gas show excellent results in a temperature range of 350–700 °C. The variation of pure hydrogen concentration at 500 °C and in H_2–N_2 gas mixture (up to 5 vol % H_2) at 400 °C shows that the fabricated sensor responds in corresponding hydrogen concentration. The sensor capability was reported to be also excellent in the presence of CH_4, C_3H_8, and C_4H_{10} gases in the

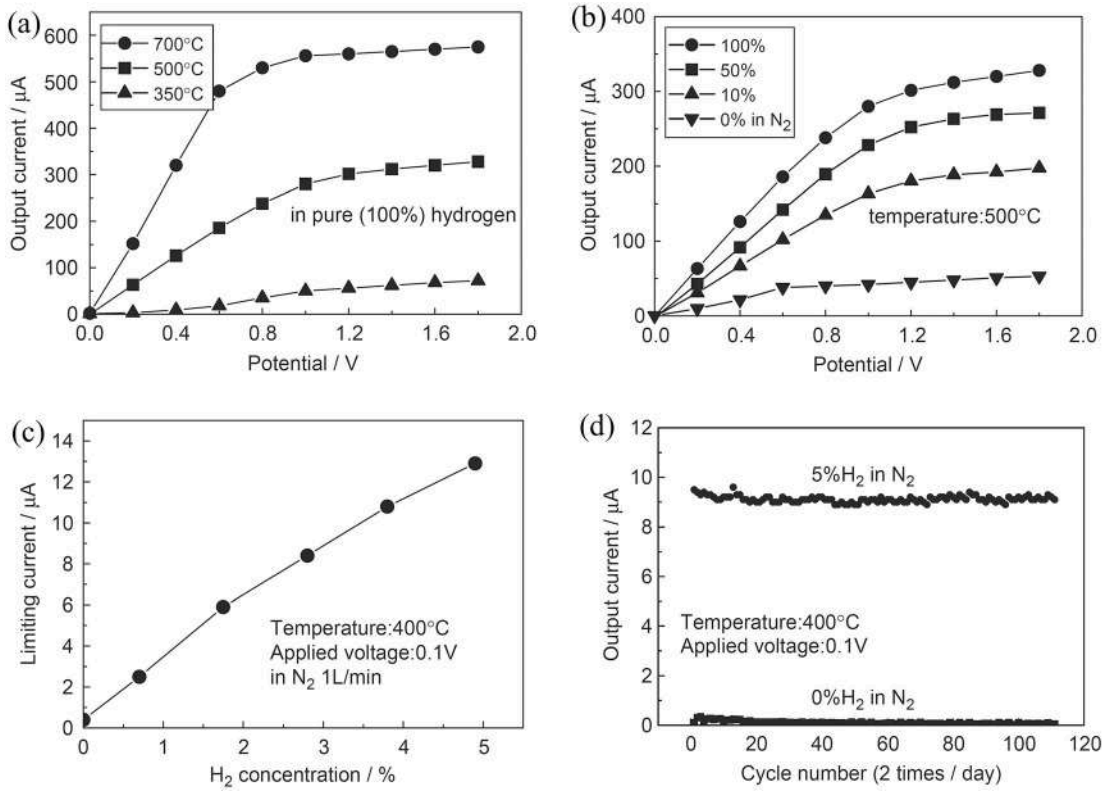

Fig. 7. Hydrogen sensor's (a) I–V characteristics in pure H_2, (b) I–V characteristics at 500 °C at different concentration of H_2, (c) dependency of limiting current on H_2 concentration at 400 °C and applied voltage 0.1 V, and (d) cycling characteristics at 400 °C and applied voltage of 0.1 V between 0 and 5% H_2 concentrations [33].

stream. From the investigation of current potential characteristics (Fig. 7 (a)), it is clear that for limiting-current hydrogen sensors, these materials could be used. At every concentration of H_2 (Fig. 7(b), the limiting currents are flat due to the contribution of electric conductivity. Moreover, limiting current raised linearly with the increase of H_2 concentration (Fig. 7(c)). Cyclic characteristics were observed which indicates that over 52 days and 100 cycles, output currents for 0% and 5% H_2 concentration does not degrade (Fig. 7(d)).

Patki et al. have studied the application of $BaZr_{0.8}Ce_{0.1}Y_{0.1}O_{3-\delta}$ based membrane for galvanic hydrogen pumping in methane dehydroaromatization reaction for in-situ separation of product hydrogen from the system [87]. They have deposited Cu on perovskite materials by electroless plating to use as anode electrode on one side and Ni–$BaZr_{0.7}Ce_{0.2}Y_{0.1}O_{3-\delta}$ cermet as a cathode. The performance of such system under gas mixture containing methane, ethane, CO, and H_2 shows that: (1) the proposed system can pump H_2 at 40 mA cm^{-2} through Cu–Cu electrodes using 268 mW/(NmL.H_2 min^{-1}), and (2) the faradaic efficiency decreases with increasing cerium content in the solid membrane structure which may due to the migration of cerium from cermet structure. In another galvanic hydrogen pump application study is reported by Tanaka et al. using $BaZr_{0.955}Co_{0.0155}Y_{0.03}O_{3-\delta}$ as a solid electrolyte membrane and platinum as an electrode [19]. The hydrogen recovery performance was analyzed in one end closed tube type set-up under a temperature of 350–550 °C. While no oxygen ion-conduction was observed in standard water vapor electrolysis condition up to 550 °C operation temperature, however, mixed conduction of proton, electron, and oxygen conduction was observed even at 425 °C of operating condition. Fig. 8(a-c) shows the characteristics of hydrogen extraction while Fig. 8(d-f) shows characteristics of hydrogen pumping. From Fig. 8(b), it is seen that in anode compartment water vapor concentration decreases with the increasing current density while in cathode compartment it remains consistent. These results show that hydrogen is produced by vapor electrolysis and conductivity of oxide-ion is nearly insignificant under wet atmosphere conditions. Fig. 8 (e) indicates that the oxide-ion went through the proton conductor and concentration increased with the increase of current density. Even at lower current density, migration of oxide-ion happened.

A hydrogen pump made out of dense $Ba(Zr_{0.30}Ce_{0.54}Y_{0.15}Cu_{0.01})O_{3-\delta}$ as a solid electrolyte where porous $BaZr_{0.75}Y_{0.03}O_{3-\delta}$ -graphite layer was tape cast on both sides of the electrolyte, and composite electrode of $(La_{0.7}Sr_{0.3})V_{0.9}O_{3-\delta}$, a trace of CeO_2, Pd was infiltrated on the porous layer was studied by Choi [88]. The hydrogen pump operation performed well when 3 wt% H_2O atm was used as sweep gas, and an over potential of 1.1 eV at 973 K for a current density of 2 A cm^{-2} was recorded. Therefore, such a composite membrane has good potential to be used in the synthesis of hydrocarbon fuels, ammonia, where in-situ hydrogen separation is needed. The attractive properties of $BaCe_{0.2}Zr_{0.7}$ $Y_{0.1}O_{3-\delta}$ composites membrane were studied by Robinson et al. [89]. In this galvanic hydrogen pump study, coated 65 wt% NiO-35 wt% $BaCe_{0.2}Zr_{0.7}Y_{0.1}O_{3-\delta}$ cermet using spray coating and porous $La_{0.6}Sr_{0.4}Fe_{0.8}Co_{0.2}O_{3-\delta}$ material by sintering as electrodes were used. The resulting device has a shell and tube form, where a gas mixture of He, H_2, H_2O was passed on the shell side, and gas mixture of Ar & H_2O was passed on the tube side of the device during performance study at a temperature range of 650 °C and 800 °C. The Galvanic hydrogen flux measured through the studied solid electrolyte membrane fits

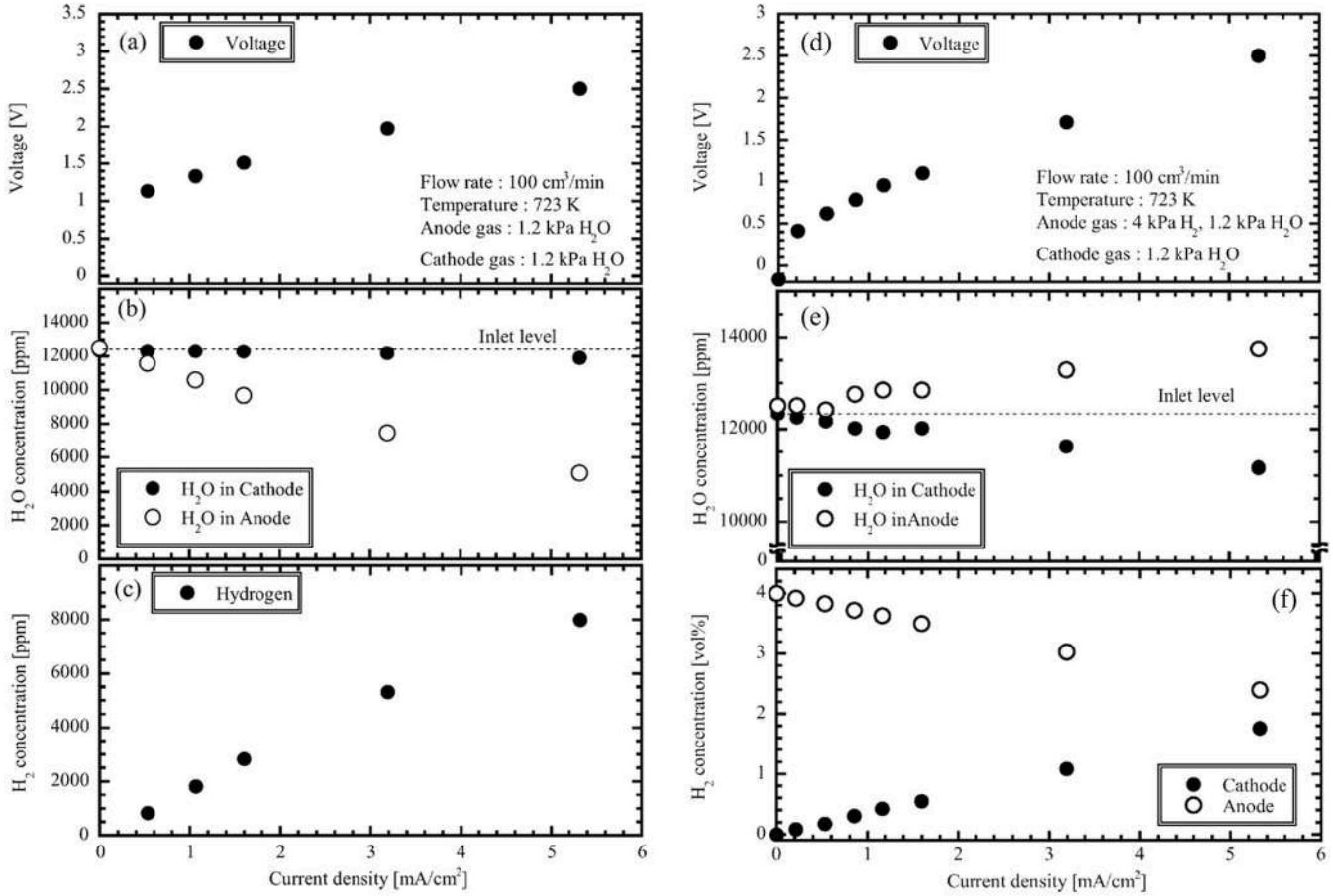

Fig. 8. Characteristics of H_2 extraction at 600 °C under wet atmosphere: (a) voltage, (b) concentration of water vapor at both anode and cathode, (c) extracted H_2 concentration at the cathode. Characteristics of H_2 pumping at 600 °C: (d) voltage, (e) concentration of water vapor at both anode and cathode, (f) extracted H_2 concentration at cathode and anode [19].

excellently with theoretical faradaic predictions. Therefore, such fabricated devices are suitable for potential applications as hydrogen pumps in a wide temperature range.

5.2. Comparative studies on fuel cell electrolytes

The electrolyte is one of the most important components in fuel cells since the operating conditions and efficiency largely depend on its characteristics [90]. Y-doped barium zirconate (BZY) has a lot of potential as a fuel cell electrolyte due to its good protonic conductivity along with higher chemical stability [91]. That is why comparative studies of various types of doped barium zirconate electrolytes are essential, which is summarized and analyzed in the following sections based on recent literature.

5.2.1. Grain growth and relative density

Grain size, grain boundary (GB), and relative density are important parameters for fuel cell electrolyte materials as they determine the performances of the fuel cell like total conductivity, power density, etc. [91–93]. Grain size and relative density mainly depend on electrolyte composition, sintering method, sintering temperature, and sintering time (Table 1). Nikodemski et al. (2013) [94] studied the mechanism of the solid-state reactive sintering (SSRS) method on $BaCe_{0.8}Y_{0.2}O_{3-\delta}$ (BCY20), $BaCe_{0.6}Zr_{0.3}Y_{0.1}O_{3-\delta}$ (BCZY63), and $BaZr_{0.8}Y_{0.2}O_{3-\delta}$ (BZY20) with NiO sintering additives. Fig. 9 (a) shows the dependency of relative density on dopant ionic radius. The dopants were categorized into three groups based on their shrinkage behavior and color pattern of the sintered pellets. Group 2 (sintering additives of metal ions with oxidation state +2) shows the highest densified electrolytes (> 90%). Fig. 9(b-d)

Table 1
Average grain size and relative density of barium zirconate electrolytes with different compositions for various synthesis methods, sintering time, and sintering temperature.

Electrolyte materials	Synthesis method	Sintering temperature (°C)	Sintering time (h)	Relative density (%)	Average grain size, D_g (μm)	Refs.
$BaZr_{0.8}Y_{0.2}O_{3-\delta}$	Citrate-nitrate combustion	1600	5	79.32	0.28	[95]
$BaZr_{0.8}Y_{0.15}Sm_{0.05}O_{3-\delta}$		1450	10	86.76	0.41	
$BaZr_{0.8}Y_{0.1}Sm_{0.1}O_{3-\delta}$		–	–	87.09	0.49	
$BaZr_{0.8}Y_{0.05}Sm_{15}O_{3-\delta}$		–	–	89.22	0.63	
$BaZr_{0.8}Sm_{0.2}O_{3-\delta}$		–	–	91.36	0.79	
$BaZr_{0.8}Y_{0.2}O_{3-\delta}$	SSRS (with Ball-milled precursor powder)	1435	5	56	0.51	[93]
			15	70	0.72	
		1485	10	82	0.88	
		1535	5	87	1.02	
			15	94	1.19	
	SSRS (with Planetary Ball-milled precursor powder)	1435	5	94	0.61	
			15	94	0.82	
		1485	5	94	0.83	
			10	94	0.93	
			15	95	0.96	
			20	95	1.04	
			25	95	1.16	
		1535	5	94	1.06	
			15	95	1.39	
$BaZr_{0.98}Y_{0.02}O_{3-\delta}$	Solid-state reactions	1700	10	95	–	[13]
$BaZr_{0.95}Y_{0.05}O_{3-\delta}$		1700		97		
$BaZr_{0.9}Y_{0.1}O_{3-\delta}$		1700		91		
$BaZr_{0.85}Y_{0.15}O_{3-\delta}$		1700		90		
$BaZr_{0.8}Y_{0.2}O_{3-\delta}$		1700		92		
$BaZr_{0.75}Y_{0.15}O_{3-\delta}$		1710		87		
$BaZr_{0.9}Sc_{0.1}O_{3-\delta}$		1700		91		
$BaZr_{0.9}In_{0.1}O_{3-\delta}$		1700		93		
$BaZr_{0.9}Gd_{0.1}O_{3-\delta}$		1650		88		
$BaZr_{0.8}Y_{0.2}O_{3-\delta}$	Combustion	1400	6	–	1	[103]
$BaZr_{0.4}Ce_{0.4}Y_{0.2}O_{3-\delta}$	SSRS	1400	8	97	5–10	[97]
$BaZr_{0.6}Ce_{0.2}Y_{0.2}O_{3-\delta}$	SSRS	1400	12	97	4–6	
$BaZr_{0.9}Y_{0.1}O_{3-\delta}$	Sonochemical	1400	20	84	–	[102]
		1450	20	90	4.63 ± 1.60	
		1500	20	95	7.67 ± 2.79	
$Ba_{1.00}Zr_{0.90}Y_{0.10}O_{3-\delta}$	SSRS	1600	8	89.23	~(0.1–1.0)	[98]
$Ba_{1.00}Zr_{0.90}Y_{0.10}O_{3-\delta}$		1600	24	92.9		
$Ba_{0.97}Zr_{0.90}Y_{0.10}O_{3-\delta}$		1600	40	93.93		
$Ba_{0.96}Zr_{0.90}Y_{0.10}O_{3-\delta}$		1600	70	94.44		
$Ba_{0.98}Zr_{0.90}Y_{0.10}O_{3-\delta}$		1600	100	96.84		
$Ba_{0.95}Zr_{0.90}Y_{0.10}O_{3-\delta}$		1600	200	97.1	–	
$BaZr_{0.85}Y_{0.15}O_{3-\delta}$	–	1450	10	–	~0.5	[91]
$BaZr_{0.5}Ce_{0.3}Y_{0.2}O_{3-\delta}$ + NiO (before calcination)	Solid-state reaction	1600	10	97	≥10	[92]
$BaZr_{0.5}Ce_{0.3}Y_{0.2}O_{3-\delta}$		1600	24	96.4	1.5	
$BaZr_{0.5}Ce_{0.3}Y_{0.2}O_{3-\delta}$ + NiO (after calcination)		1600	10	96.4	5	
$BaZrO_3$ + ^{134}BaO	Spray pyrolysis	1600	10	>97%	1.1 ± 0.1	[104]
$BaZrO_3$ + ^{96}ZrO						
$BaZr_{0.9}Y_{0.1}O_{2.95}$ (Exsolve Composite)	Spray pyrolysis	1600	10	–	$(4.5 \pm 1.4) \times 10^{-2}$	[101]
$BaZr_{0.9}Y_{0.1}O_{2.95}$					$(6.2 \pm 2.4) \times 10^{-2}$	
$BaZr_{0.9}Y_{0.1}O_{3-\delta}$	Gel-polymerization	–	–	–	$(4–5) \times 10^{-2}$	[105]
$BaZr_{0.9}Y_{0.1}O_{3-\delta}$	Combustion-based wet-chemical route	1500–1600	12	95	$(6–12) \times 10^{-2}$	[99]
$BaZr_{0.9}Y_{0.1}O_{3-\delta}$	Gel-pol	–	–	–	$(4–7) \times 10^{-2}$	[100]

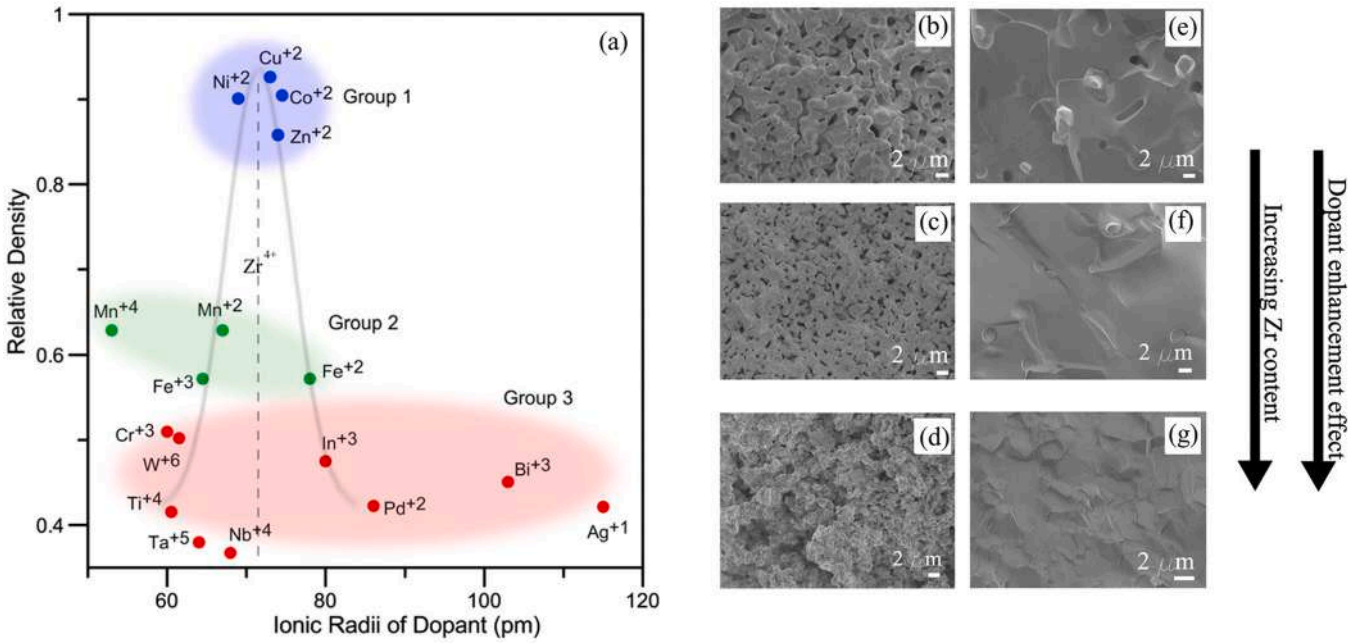

Fig. 9. (a) Relation between ionic radius and relative density using SSRS method sintered at 1450 °C for 12 h. Cross-sectional SEM images of **(b)** BCY20 sintered for 12 h at 1400 °C (relative density ~59.7%), **(c)** BCZY63 sintered for 12 h at 1500 °C (relative density ~60%), **(d)** BZY20 sintered for 12 h at 1500 °C (relative density ~34.1%), **(e)** BCY20 + 5 mol% NiO sintered for 12 h at 1400 °C (relative density ~98.6%), **(f)** BCZY63 + 5 mol% NiO sintered for 12 h at 1500 °C (relative density ~90%), and (g) BZY20 + 5 mol% NiO sintered for 12 h at 1500 °C (relative density ~95.1%) [94].

shows SEM images of BCY20, BCZY63, BZY20, whereas Fig. 9(e-g) shows SEM of with the addition of NiO. It is understood from the figures that the increase of Zr content, grain size, and density decrease, which indicates that yttrium doped barium zirconate without Ce has poor sintering behavior. However, adding 5% NiO can significantly improve the sinterability and densify the electrolyte, which proves that NiO mitigates the poor sintering properties of zirconium.

Table 1 focused on the average grain growth and relative density of different doped and co-doped barium zirconate electrolytes. Z. Zhu and S. Wang (2019) [95] investigated the BZY electrolyte with Sm^{3+} co-doping and found out the dependency of average grain size with the co-doping level. It is seen from their data that grain size and relative density increase with the increase of Sm^{3+} incorporation. Irshad et al. (2019) [96] also pointed out that using Sm^{3+} or Gd^{3+} can lower the average grain size. Using Sm^{3+} lowers the grain size to the later one. But it is noticed that the grain size of pure BZY has the smallest grain size among the other studies. The work of Jeong et al. (2018) [97] proves that increasing Ce molar percentage in BZY can lead to a larger grain size. On the other hand, J. Bu, P. G. Jönsson, and Z. Zhao [92] found that adding NiO before calcination to the electrolyte can increase the mean grain size due to its higher density. Yun et al. (2018) [93] used a different approach and studied the effect of the sintering process, temperature, and time on the grain size. It was observed that the range of average grain size (0.61–1.39 μm) using planetary ball-milled precursor powder is higher than the grain size (0.51–1.19 μm) using only ball-milled precursor powder. It is also clear that in both cases, grain size increases with the increase of sintering temperature and time (Fig. 10).

From Han and Uda's work [98] it is also observed that relative density depends on the sintering time. Relative density rises to 95% after sintering for 100 h. The grain size was found in the micro-meter range from this study. On the other hand, Chen et al. (2018) [99], Hosseinabadi et al. (2019) [100], Rioja-Monllor et al. (2019) [101] have found the lowest grain size, in 10^{-2} μm range, for BZY10 electrolytes. It was not clear whether the lowest grain size is due to the electrolyte composition or not. However, Seeharaj et al. (2016) [102] used the sonochemical method and found the highest grain size. The average grain size of BYZ ceramics sintered at 1550 °C was 7.67 ± 2.79 μm, which is significantly larger than pure BYZ ceramics. Therefore, the authors suggested increasing grain size diameter for reducing grain boundary resistivity to improve the performance of proton conductivity.

5.2.2. *Activation energy*

The activation energy for proton conductivity and diffusivity are important parameters of a solid oxide fuel cell electrolyte. Generally, the lower activation energy for proton conductivity means fuel cells can operate at a lower temperature [12]. Solid oxide fuel cells (SOFCs) need high operating temperature due to their higher activation energy for conductivity, while protonic oxide fuel cells can operate at a lower temperature because of their lower activation energy for conductivity [12,101]. Table 2 recaps the data of activation energies for proton conductivity for the different compositions of BZY at various temperature ranges and atmospheres. According to the study of Jarry et al. (2018) [106], the activation energy for conductivity decreases with the increase of Ce doping. Zhu and Wang (2019) [95] examined the activation energy for the conductivity of Sm^{3+} doping BZY in wet air and wet hydrogen. The activation energy for conductivity in a wet hydrogen atmosphere (0.28–0.31 eV) is three times lower than in wet air (0.94–0.97 eV). This is because, in the hydrogen atmosphere, the proton acts as the majority current carrier whereas electron holes and oxygen ions contribute to conductivity in wet air oxygen. It is also noticed that with the increase of Sm^{3+} doping activation energy for conductivity increases in both wet air and wet hydrogen atmospheres. This result is also supported by the work of Zhu et al. (2019) [107]. Huang et al. (2018) [108] investigated apparent activation energy for conductivity in four different atmospheres and found consistent results. However, activation energy in a hydrogen atmosphere (0.157 eV) is lower than the typical energy value (0.417 eV) for proton conductivity, especially in dry hydrogen which might be caused by the *porous/dense/porous* structure of integrated electrolyte matrix. Fluri et al. (2017) [109] concluded that in dry oxygen activation energy for conductivity is higher because the electron holes act as dominant charge carrier. On the other hand, due to proton conductivity in a humidified argon atmosphere and relaxed structure of the lattice, activation energy is less. There is an inversely proportional relationship between activation

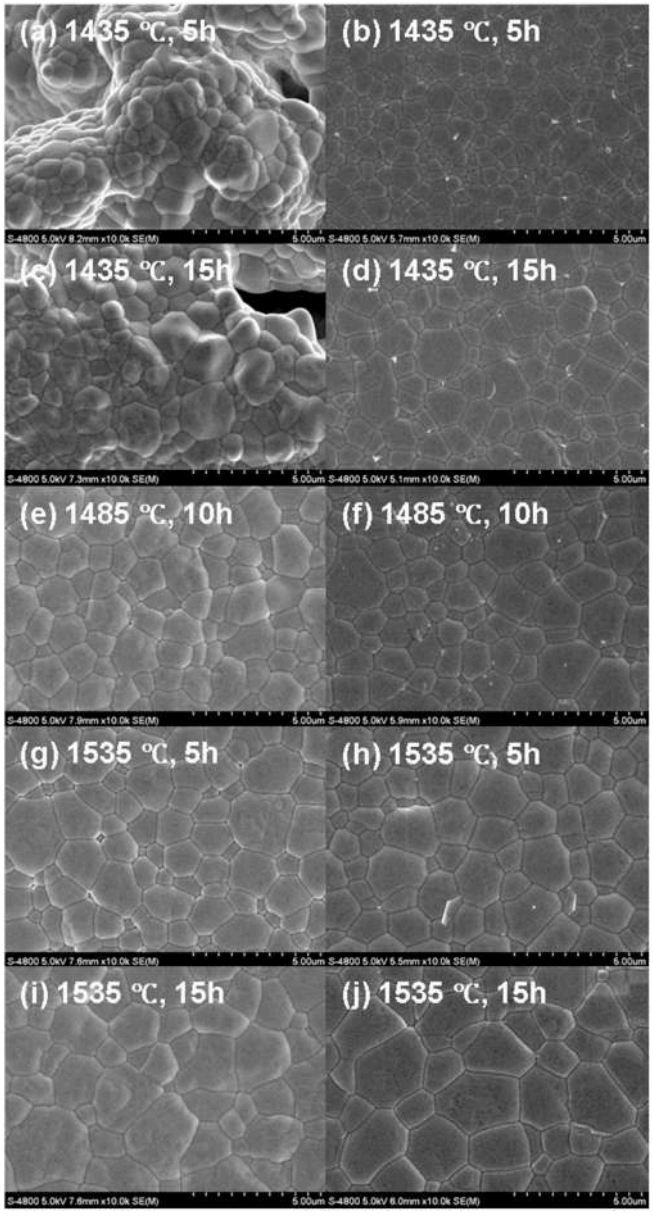

Fig. 10. SEM images of BZY electrolyte using (left) ball-milled and (right) planetary ball-milled precursor powder sintered at different temperatures for a different time period [93].

energy and tensile strain was also found. Besides, no correlation exists between the activation energy and electrolyte thickness.

Activation energies for different types of diffusion (tritium diffusion, protonic diffusion, conductivity diffusion, etc.) are summarized in Table 3. Sažinas et al. (2017) [104] studied the activation energy for lattice and grain boundary (GB) diffusion of BaO and ZrO in barium zirconate electrolyte and pointed out that activation energy is higher for lattice diffusion than for grain boundary diffusion. Noferini et al. (2018) [113] studied different types of the standard diffusion model to estimate activation energy and reported that 10% In doped barium zirconate ($BaZr_{0.8}In_{0.2}O_{2.9}$) exhibits lower activation energy for diffusion than 20% In doping ($BaZr_{0.8}In_{0.2}O_{2.9}$) across all the model.

Kreuer et al. (2000) [13] pointed out that activation energy for conductivity diffusion is higher than the activation energy for proton diffusion. On the other hand, Fig. 11 (a) illustrates that the lowest activation energy (0.43 eV) of proton diffusivity is noticed for 10% Y doping while 10% Sc doping barium zirconate has the highest activation energy (0.50 eV). However, among the different Y doping concentrations **(Fig. 11 (b))**, 20% doped electrolyte has slightly increased activation energy (0.48 eV), which, according to the authors, might be due to the lattice distortion by Y dopant. Raiteri et al. (2011) [114] pointed out that for both Y doped and pure barium zirconate electrolyte, the Arrhenius plots of proton diffusivity are parallel **(Fig. 11 (c))**, which indicates that Y-doping of little concentration does not affect the activation energy for proton diffusion. Recent studies [80,115] stated that the tritium diffusivity in both $BaZr_{0.9}Y_{0.1}O_{3-\delta}$ (BZY) and $BaZr_{0.955}Y_{0.03}Co_{0.015}O_{3-\delta}$ (BZYC) increases with the increase of temperature, as shown in Fig. 11(d). However, at a higher temperature (1000 °C) both samples show similar diffusivity value, whereas at lower temperature (400 °C) diffusivity of BZY (2×10^{-12} m^2/s) is one order lower than the BZYC (4×10^{-11} m^2/s).

Table 4 summarizes the data of activation energy for the resistance of different compositions of barium zirconate. Wu et al. (2019) [116] found out that with the increase of Fe-doping, the activation energy of polarization resistance for each composition does not vary due to the different reaction steps at the electrodes. This study concluded that $BaZr_{0.2}Fe_{0.6}Y_{0.2}O_{3-\delta}$ (BZFY-6) has the lowest activation energy (0.946 eV), and therefore, it is more useful and beneficial at low temperatures. Jeong et al. (2018) [97] conducted a similar kind of experiment with Ce doping. Using a different composition of Ce doping, a change in activation energy for polarization resistance (R_p) was observed, which implies that the cathodic reaction involves the same rate-determining steps. On the other hand, Rioja-Monllor et al. (2019) [101] reported that activation energy for area-specific resistances (ASRs) is lower in a moist atmosphere than in dry air. Besides, when the electrolyte composition was made by exsolution, the activation energy was found lower than the direct composition.

5.2.3. Total conductivity

BZY10 shows mixed bulk conductivity, like, protonic defect conductivity, electronic conductivity, and oxygen vacancy conductivity, among which protonic conductivity dominated about 98.5% of conductivity up to 600 °C operating temperature [119]. Protonic defects are involved with hydration reaction [$H_2O\ (g) + O_o^{\times} + V_o^{\bullet\bullet} \leftrightarrow 2OH_o^{\bullet}$] which is largely associated with the near-surface lattice structure and surface vacancies ($V_o^{\bullet\bullet}$) to adsorb the water (H_2O) [12,120–122]. Conventional measurement techniques like proton-NMR [123], TGA [12,120,122], Raman profilometry [124], and HT-XRD [125–127] can determine the bulk protonic defects ($OH_o^{\bullet}$) in the BZY10 crystal, but to understand the near-surface and surface chemistry, a special technique like ambient-pressure X-ray photoelectron spectroscopy (AP-XPS) is required [106,128].

Ling et al. (2016) [129] reported that acceptor-doped $BaZrO_3$ oxides are more suitable for practical application, e.g., proton-conducting solid oxide fuel cells (H–SOFCs) due to their acceptable conductivity. However, significant sintering activity is a problem and requires doping with trivalent cations. The authors studied the effect of co-addition of Bi_2O_3 and In_2O_3 on sintering behavior and electrical properties of $BaZr_{0.8-x}In_{0.2}Bi_xO_{3-\delta}$ (x = 0, 0.05, 0.1, and 0.2). Among those four compositions, $BaZr_{0.8-x}In_{0.2}Bi_xO_{3-\delta}$ (x = 0.05), i.e., BZIB5, exhibited the highest conductivity of 9.93×10^{-4} Scm^{-1} at 600 °C, outstanding electrochemical performance with a maximum power density of $0.34Wcm^{-2}$ at 700 °C. Bi doping increased the power density by 300%. Furthermore, the addition of Bi concentration increased the activation energy (E_a). Compared to Y-doped $BaZrO_3$, In-doped $BaZrO_3$ results in superior conductivity and grain boundary. The authors reported that BZIB5 is a suitable electrolyte material for H–SOFCs.

Zhu et al. (2019) [107] also stated that $BaZrO_3$ oxides have excellent chemical stability in CO_2 or H_2O-containing environments. However, there is a significant challenge in film densification and grain growth due to high grain boundary density and low conductivity. The authors co-doped Ca^{2+} and Y^{3+} in the B site to improve the performance. The

Table 2
Activation energy for the conductivity of barium zirconate electrolyte with different compositions for various atmospheres and temperature ranges.

Electrolyte materials	Synthesis method	Atmospheres	Temperature range (°C)	Activation energy for	E_a (eV)	Refs.
$BaZr_{0.8}Y_{0.2}O_{3-\delta}$	Citrate-nitrate combustion	Wet H_2	300–700	Conductivity	0.28	[95]
		Wet air	400–700		0.96	
$BaZr_{0.8}Y_{0.15}Sm_{0.05}O_{3-\delta}$		Wet H_2	300–700		0.30	
		Wet air	400–700		0.94	
$BaZr_{0.8}Y_{0.1}Sm_{0.1}O_{3-\delta}$		Wet H_2	300–700		0.31	
		Wet air	400–700		0.96	
$BaZr_{0.8}Y_{0.05}Sm_{0.15}O_{3-\delta}$		Wet H_2	300–700		0.30	
		Wet air	400–700		0.97	
$BaZr_{0.8}Y_{0.15}Ca_{0.05}O_{3-\delta}$	Citrate-nitrate combustion	Wet H_2	300–750	Conductivity	0.38	[107]
$BaZr_{0.8}Y_{0.15}Ca_{0.05}O_{3-\delta}$		Wet air			0.97	
$BaZr_{0.8}Y_{0.20}O_{3-\delta}$		Wet H_2			0.40	
$BaZr_{0.8}Y_{0.20}O_{3-\delta}$		Wet air			0.99	
$BaZr_{0.8}Y_{0.2}O_{3-\ \delta}$	SSRS	Wet air	400–600	Conductivity	0.602	[108]
		Dry air			0.608	
		Wet H_2			0.417	
		Dry H_2			0.157	
$BaZr_{0.8}Y_{0.2}O_{3-\delta}$	Combustion	Wet H_2 (3% H_2O)	~ (550–650)	Conductivity	0.48	[103]
$BaZr_{0.9}Y_{0.1}O_{3-\delta}$	Sol-gel	H_2	450–550	Conductivity	0.23	[110]
$BaZr_{0.9}Y_{0.1}O_{3-\delta}$ (calcined: 900 °C/4 h)	Oxidant peroxide	Air	~ (350–550)	Conductivity	0.38	[111]
$BaZr_{0.9}Y_{0.1}O_{3-\delta}$ (calcined: 1200 °C/2 h)		Air	~ (400–550)		0.39	
$BaZr_{0.9}Y_{0.1}O_{3-\delta}$ (calcined: 900 °C/4 h)		N_2	~ (350–550)		0.38	
$BaZr_{0.9}Y_{0.1}O_{3-\delta}$ (calcined: 1200 °C/24 h)		N_2	~ (250–550)		0.38	
$BaZr_{0.9}Y_{0.1}O_{2.95}$	Standard solid-state reaction	Moist air	300–500	Conductivity	0.79	[106]
$BaCe_{0.2}Zr_{0.7}Y_{0.1}O_{2.95}$					0.63	
$BaZr_{0.8}Y_{0.2}O_3$	–	dry O_2	200–325	Conductivity	0.78 ± 0.01	[109]
		Humidified Ar			0.44	
$BaZr_{0.53}In_{0.47}O_{3-\delta}$ (hydrated structure)	–	Wet air	260–340	Proton conductivity	0.44	[112]
$BaZr_{0.4}Ce_{0.4}Y_{0.2}O_{3-\delta}$	SSRS	Ar (10% H_2)	550–700	Proton conductivity	0.26	[97]
$BaZr_{0.6}Ce_{0.2}Y_{0.2}O_{3-\delta}$					0.33	
$BaZr_{0.7}Ce_{0.1}Y_{0.2}O_{3-\delta}$					0.34	
$BaZr_{0.8}Y_{0.2}O_{3-\delta}$					0.22	

Table 3
Activation energy for the diffusion of barium zirconate electrolyte with different compositions for various atmospheres and temperature ranges. (GB = grain boundary, CEM= Chudley–Elliot model, SSM= Singwi and Sjölander Model, HRM= Hall and Ross Model).

Electrolyte materials	Synthesis method	Temperature range (°C)	Activation energy for	E_a (eV)	Refs.
$BaZr_{0.9}Y_{0.1}O_{3-\delta}$	Solid-state reactions	350–600	Tritium diffusion	0.74	[115]
$BaZr_{0.955}Y_{0.03}Co_{0.015}O_{3-\alpha}$			Tritium diffusion	0.43	
$BaZr_{0.98}Y_{0.02}O_{3-\delta}$	Solid-state reactions	~ (90–325)	Protonic diffusion	0.44	[13]
$BaZr_{0.95}Y_{0.05}O_{3-\delta}$		~ (70–290)	Protonic diffusion	0.44	
$BaZr_{0.9}Y_{0.1}O_{3-\delta}$		~ (40–150)	Protonic diffusion	0.43	
$BaZr_{0.8}Y_{0.2}O_{3-\delta}$		~ (50–150)	Protonic diffusion	0.48	
$BaZr_{0.9}Sc_{0.1}O_{3-\delta}$		~ (90–200)	Protonic diffusion	0.50	
$BaZr_{0.9}In_{0.1}O_{3-\delta}$		~ (80–325)	Protonic diffusion	0.48	
$BaZr_{0.9}Gd_{0.1}O_{3-\delta}$		~ (30–110)	Protonic diffusion	0.47	
$BaZr_{0.95}Y_{0.05}O_{3-\delta}$		–	Conductivity diffusion	1.04	
$BaZr_{0.9}Y_{0.1}O_{3-\delta}$		–	Conductivity diffusion	1.00	
$BaZr_{0.85}Y_{0.15}O_{3-\delta}$		–	Conductivity diffusion	0.86	
$BaZr_{0.8}Y_{0.2}O_{3-\delta}$		–	Conductivity diffusion	0.93	
$BaZr_{0.75}Y_{0.25}O_{3-\delta}$		–	Conductivity diffusion	0.87	
$BaZr_{0.9}Sc_{0.1}O_{3-\delta}$		–	Conductivity diffusion	0.89	
$BaZr_{0.9}In_{0.1}O_{3-\delta}$		–	Conductivity diffusion	0.99	
$BaZr_{0.9}Gd_{0.1}O_{3-}$		–	Conductivity diffusion	0.99	
$BaZrO_3$ $+^{134}BaO$	Spray pyrolysis	1015–1200	Diffusion of Ba (lattice)	4.1 ± 0.5	[104]
			Diffusion of Ba (GB)	3.1 ± 0.5	
$BaZrO_3$ $+^{96}ZrO$		1300–1500	Diffusion of Zr (lattice)	4.5 ± 0.7	
			Diffusion of Zr (GB)	3.7 ± 0.4	
$BaZr_{0.9}In_{0.1}O_{2.95}$	–	–	Diffusion (CEM)	0.04	[113]
			Diffusion (SSM)	0.04	
			Diffusion (HRM)	0.04	
$BaZr_{0.8}In_{0.2}O_{2.9}$	–	–	Diffusion (CEM)	0.12	
			Diffusion (SSM)	0.11	
			Diffusion (HRM)	0.114	

authors reported a highly dense film surface of $BaZr_{0.8}Y_{0.15}Ca_{0.05}O_{3-\delta}$ (BZYC5), the grain size and thickness were 0.5–1 μm and 15 μm, respectively. The authors reported a higher total conductivity of BZYC5 compared to that of BZY. However, the activation energy for BZYC5 and BZY in wet H_2 and wet air was similar. BZYC5 exhibited better sintering activity, higher proton conductivity, and high chemical stability

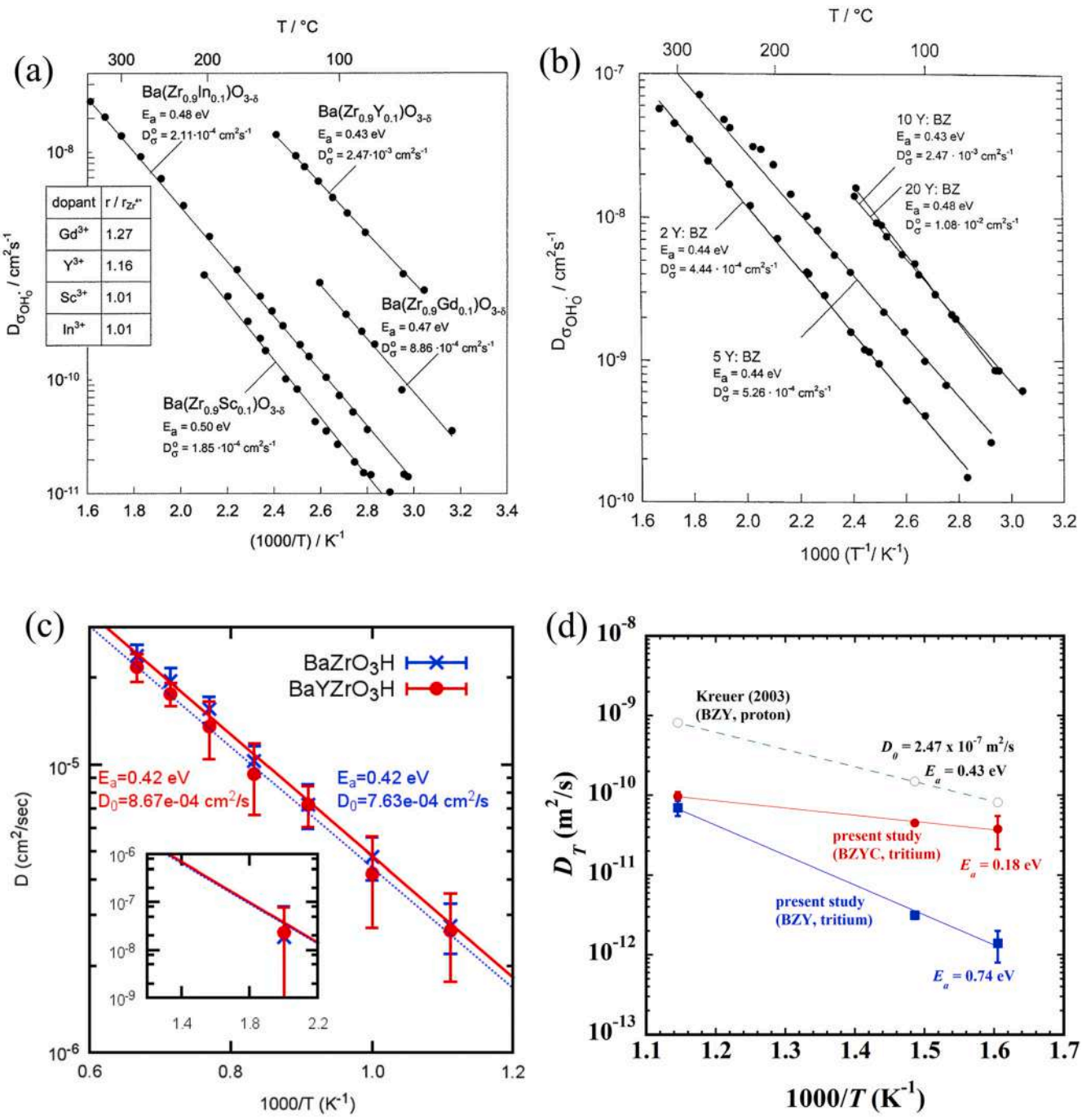

Fig. 11. Arrhenius plot of proton diffusivity of barium zirconate with **(a)** different types of dopants, and **(b)** different concentration of yttrium doping [13], **(c)** pure and Y doped barium zirconate [114], and **(d)** tritium diffusivity in BZY (blue square) and BZYC (closed red circle) [115]. (For interpretation of the references to color in this figure legend, the reader is referred to the Web version of this article.)

compared to BZY. The authors concluded that BZYC5 is a steady promising alternate proton-conducting electrolyte material.

Pure $BaZrO_3$ shows lower conductivity in the range of 10^{-6} S cm^{-1} [130], whereas in the rare earth materials (Y, Sm, Gd, etc.) doped $BaZrO_3$ show higher order of total conductivity (10^{-3} Scm^{-1} range). This is because doping with impurities leads to lowering the activation energy. Among these impurities, the yttrium doped one (BZY) shows the most promising result. Conductivity also depends on the chemical composition and sintering temperature, cell operating temperature, and atmosphere, which can be observed from Table 5. Yun et al. (2018) [93] found that when BZY is sintered at 1485 °C for 15 h, it exhibits the highest total conductivity (2.28×10^{-3} Scm^{-1}) relative to 1435 °C (1.15×10^{-3} Scm^{-1}) or 1525 °C (2.01×10^{-3} Scm^{-1}) in the atmosphere of Ar (3%H_2, $p_{H_2O} = 0.03$ atm) at 500 °C. It is noted from Fig. 12(a) that the Arrhenius plot of all the BZY compositions changes the slope at 550 °C due to the lower concentration of protons. The authors concluded that using NiO additives has little influence on the total proton conductivity of the electrolyte. Fig. 12(b) presents that grain-boundary conductivities are significantly lower than bulk conductivities due to the high amount of NiO additives. Measured and theoretical EMF values and their ratio (ion transport number) are shown in Fig. 12(c). It is clear that from 600 to 900 °C ion transport number decreases due to the lowering concentration of proton with the increase of temperature.

Huang et al. (2018) [108] reported that BZY in dry H_2 shows less

Table 4
Activation energy for resistance of barium zirconate electrolyte with different compositions for various atmospheres and temperature ranges.

Electrolyte materials	Synthesis method	Atmospheres	Temperature range (°C)	Activation energy for	E_a (eV)	ref
$BaZr_{0.4}Ce_{0.4}Y_{0.2}O_{3-\delta}$	SSRS	Ar (10% H_2)	550–700	Polarization resistance	0.94	[97]
$BaZr_{0.6}Ce_{0.2}Y_{0.2}O_{3-\delta}$					0.90	
$BaZr_{0.7}Ce_{0.1}Y_{0.2}O_{3-\delta}$					0.89	
$BaZr_{0.8}Y_{0.2}O_{3-\delta}$					0.81	
$BaZr_{0.6}Fe_{0.2}Y_{0.2}O_{3-\delta}$	Wet chemical	Wet H_2	~ (550–700)	Polarization resistance	0.954	[116]
$BaZr_{0.4}Fe_{0.4}Y_{0.2}O_{3-\delta}$					1.06	
$BaZr_{0.2}Fe_{0.6}Y_{0.2}O_{3-\delta}$					0.946	
$BaZr_0Fe_{0.8}Y_{0.2}O_{3-\delta}$					1.09	
$BaZr_{0.9}Y_{0.1}O_{2.95}$ (Composite by exsolution)	Spray pyrolysis	Dry air	–	Area specific resistance (ASR)	1.36	[101]
		3% moist synthetic air			0.60	
$BaZr_{0.9}Y_{0.1}O_{2.95}$ (Direct Composite)		Dry air			1.49	
		3% moist synthetic air			0.77	
$BaZr_{0.9}Y_{0.1}O_{2.95}$	–	–	23–277	Quasi-elastic component (Proton Transfer)	0.09 ± 0.05	[117]
				Quasi-elastic component (O–H rotation)	0.08 ± 0.05	
$BaZr_{0.9}Sc_{0.1}O_{2.95}$				Quasi-elastic component (Proton Transfer)	0.096 ± 0.02	
				Quasi-elastic component (O–H rotation)	0.1 ± 0.02	
$BaZr_{0.8}Y_{0.2}O_{3-\delta}$	–	90% humid air	23–177	Time constant (Annealed Sample)	0.55	[118]
				Time constant (Virgin Sample)	0.65	

conductivity than in wet H_2. Gonçalves et al. (2016) [111] synthesized BZY using the oxygen peroxide method in two different atmospheres, namely in N_2 and in laboratory air. 120 times improvement of conductivity was found in the N_2 atmosphere over the air due to the denser sintered pellets. Ling et al. (2016) [129] observed that with the increase of cell operating temperature, conductivity increases. Similar results were supported by the study of Xiao et al. (2016) [131] as well as Xie et al. (2018) [132]. Ce is a very common co-doping substrate to BZY, which can increase the conductivity of the electrolyte. Jarry et al. (2018) [106] found relatively high conductivity using Ce and Zr co-doping. $BaCe_{0.9}Y_{0.1}O_{2.95}$ (BZY) has poor grain boundary conductivity, while $BaCe_{0.9}Y_{0.1}O_{2.95}$ (BCY) has lower chemical stability. To resolve these problems, the authors used Ce and Zr co-doped barium zirconate as an electrolyte. Jeong et al. (2018) [97] reported that $BaZr_xCe_{0.8-x}Y_{0.2}O_{3-\delta}$ (BCZY) (where x = 0.4, 0.6, 0.7, and 0.8) in Ar (10% H_2) atmosphere with the increase of Ce co-doping (0%–40%) the conductivity increases almost double. J. Bu et al. [92] one step further and studied the effect of NiO incorporation in a different stage of the calcination process of BCZY. Based on this study, it is concluded that adding NiO before calcination showed the best-enhanced oxygen and proton conductivities, followed by adding NiO after calcination and no addition of NiO. So, adding NiO during the synthesis process helps to increase the conductivity and lower the sintering temperature of BZCY electrolytes. However, Chen et al. (2018) [110] found the highest conductivity in the BZY electrolyte in the order of 10^{-1} S cm^{-1}. The conduction mechanism might be different and found out that pure oxygen conduction is the main reason for high conductivity [110].

5.2.4. Peak power density

Though indium-doped $BaZrO_3$ (BZI) shows lower proton conductivity than the yttrium-doped $BaZrO_3$ (BZY) [141], the BZI has higher chemical stability in the CO_2 atmosphere and better sintering ability as well [142]. Moreover, indium and yttrium co-doped $BaZrO_3$ cell [143], and indium and bismuth co-doped $BaZrO_3$ cell [129] show higher power density than the BZI cell [142]. Therefore, it was postulated that by the addition of a dopant in the BZI, the cell performance could be improved.

In Table 6, performances of the fuel cell, namely peak power density (P_{max}), open-circuit voltage (OCV) with polarization resistance (R_p), and ohmic resistance (R_Ω) are summarized. Electrochemical impedance spectroscopy (EIS) is conducted on the single-cell under open-circuit conditions to measure ohmic resistance and polarization of electrolyte materials [95]. Open circuit voltage is calculated by Nernst equation [138,144,145]. From Zhu and Wang's [95] study, it is noticed that with the increase of operating temperature from 600 °C to 700 °C, peak power density doubles due to the lower polarization resistance. In this study, 5% of Sm is co-doped with BZY. Ling et al. (2016) [129] studied indium and bismuth co-doping in barium zirconate and found relatively higher peak power density (340 $mWcm^{-2}$) at 700 °C, which is about 3 times higher than only indium doping barium zirconate. Besides, the OCV value is also higher than the barium zirconate electrolyte, which indicates that bismuth doping increases the density of the electrolyte, and electron conduction can be ignored.

Zhu et al. (2019) [107] investigated calcium and yttrium doping and found out that Ca and Y doping in barium zirconate shows comparable performance with other researchers' works [137,142,146–148]. From the SEM image of $BaZr_{0.8}Y_{0.15}Ca_{0.05}O_{3-\delta}$ (BZYC5) shown in Fig. 13(a and b), it can be noted that the electrolyte has a lower number of pores and highly dense, which improves the proton transfer by reducing ohmic resistance. However, OCV values are lower (Fig. 13(c)) than the theoretical value, and this result is due to the fact of hole conduction at high operating temperature. Fig. 13(d) presents that ohmic resistance (intercept of the spectra in the real axis at high frequency) and polarization resistance (the difference between low and high-frequency intercept at real axis) significantly increases if the operating temperature decreases. Yun et al. (2018) [93] also found comparable power density values, which is illustrated in Fig. 12(d).

Dai (2017) stated in his study [137] that with co-doping 5% of Pr exhibits better cell performance than 10% Pr co-doping. Bi et al. (2017) [103] found quite higher peak power density in BZY electrolyte, which is mainly caused by the use of BZY-NiO anode substrate. Irshad et al. (2019) [96] used Y, Gd, Sm doping and found comparable peak power density, but P_{max} of Gd doping composition was relatively lower than the other two. Fuel cells based on $BaZr_{0.8}Sm_{0.2}O_{3-\delta}$ (BZSm) and $BaZr_{0.8}Gd_{0.2}O_{3-\delta}$ (BZGd) electrolyte shows smaller peak power density (320 $mWcm^{-2}$, 240 $mWcm^{-2}$) as compared to $BaZr_{0.8}Y_{0.2}O_{3-\delta}$ (BZY) electrolyte (340 $mWcm^{-2}$). This is because of the mixture of dopants when they split over the A and B sites of perovskite. However, BZSm shows higher peak power density relative to BZGd due to its dense structure, which limits the gas diffusion and increases the fuel cell performance. Moreover, BaO deteriorates the performance of BZSm and BZGd. Therefore, if the sintering temperature is increased, the BaO phase will be removed, which will increase the power density. Xie et al. (2018) [132] studied Gd–Zn co-doping in barium zirconate to enhance cell performance. The maximum power obtained in the study is higher

Table 5
Total conductivity of barium zirconate electrolyte materials with different compositions for various synthesis methods, sintering conditions, and measurement atmosphere.

Electrolyte materials	Synthesis method	Sintering temperature (°C)/ time (h)	T (°C)/atmosphere	Total conductivity, σ (S cm^{-1})	Ref.
$BaZr_{1-x}Y_xO_{3-\delta}$ (x = 0.1–0.25)	Solid state rection	1600/24	500/wet H_2 (p_{H_2O}= 0.05 atm)	~(0.001–0.019)	[90]
			600/wet H_2 (p_{H_2O}= 0.05 atm)	~(0.002–0.029)	
			700/wet H_2 (p_{H_2O}= 0.05 atm)	~(0.003–0.024)	
$BaZr_{0.8}Y_{0.2}O_{3-\delta}$	Solid state rection	1600/24	500/wet O_2 (p_{H_2O}= 0.05 atm)	~0.019	
			600/wet O_2 (p_{H_2O}= 0.05 atm)	~(0.029–0.035)	
			700/wet O_2 (p_{H_2O}= 0.05 atm)	(~0.025–0.06)	
$BaZrO_3$	SSR	1600/12	600/wet N_2	2.21×10^{-6} 7.64×10^{-7}	[130]
$BaZr_{0.9}Y_{0.1}O_{3-\delta}$	Gel polymerization	–	80/wet air (95% RH)	1.26×10^{-5}	[105]
$BaZr_{0.8}Y_{0.2}O_{3-\delta}$	Combustion	1400/6	600/wet H_2 (3% H_2O)	4.5×10^{-3}	[103]
$BaZr_{0.8}Y_{0.2}O_{3-\delta}$	Combustion	1150/4	650/wet H_2 (3% H_2O)	2.2×10^{-3}	[96]
$BaZr_{0.9}Y_{0.1}O_{3-\delta}$	SSRS	1640/15	600/H_2O-saturated N_2	2.14×10^{-3}	[133]
$BaZr_{0.85}Y_{0.15}O_{3-\delta}$	Solid state reaction	1400/10	600/wet N_2 600/wet N_2	1.5×10^{-3} 8.7×10^{-4}	[134]
$BaZr_{0.8}Y_{0.2}O_{3-\delta}$	SSRS	1400/8	700/wet air	6.9×10^{-3}	[135]
$BaZr_{0.85}Y_{0.15}O_{3-\delta}$	–	1600/10	600/wet N_2 (3% H_2O)	3.9×10^{-3}	[136]
$BaZr_{0.9}Y_{0.1}O_{3-\delta}$	Oxidant peroxide	1200/24	900/Air 1200/Air 900/N_2 1200/N_2	4.5×10^{-5} 1.0×10^{-5} 1.13×10^{-3} 1.20×10^{-3}	[111]
$BaZr_{0.53}In_{0.47}O_{3-\delta}$ (hydrated structure)	–	–	300/wet air	9.2×10^{-4}	[112]
$BaZr_{0.8}Y_{0.15}Sm_{0.05}O_{3-\delta}$	Citrate-nitrate combustion	1450/10	600/wet H_2 700/wet H_2	1.36×10^{-3} 2.48×10^{-3}	[95]
$BaZr_{0.75}In_{0.2}Bi_{0.05}O_{3-\delta}$	Citric acid - EDTA	1500/10	700/wet H_2 (~3% H_2O) 650/wet H_2 (~3% H_2O) 600/wet H_2 (~3% H_2O)	3.0×10^{-3} 2.3×10^{-3} 1.5×10^{-3}	[129]
$BaZr_{0.8}Y_{0.20}O_{3-\delta}$ $BaZr_{0.8}Y_{0.15}Ca_{0.05}O_{3-\delta}$	Citrate-nitrate combustion	1600/10	600/wet H_2 600/wet H_2	4.6×10^{-4} 8.0×10^{-4}	[107]
$BaZr_{0.8}Y_{0.2}O_{3-\delta}$	SSRS	1435/15 1485/15 1535/15 1435/15 1485/15 1535/15	500/Ar (3%H_2, p_{H_2O} = 0.03 atm) 600/Ar (3%H_2, p_{H_2O} = 0.03 atm)	1.15×10^{-3} 2.28×10^{-3} 2.01×10^{-3} 3.0×10^{-3} 3.0×10^{-3} 1.24×10^{-3}	[93]
$BaZr_{0.75}Y_{0.2}Pr_{0.05}O_{3-\delta}$	Sol-gel	1650/10	600/wet air (~3% H_2O)	2.0×10^{-3}	[137]
$BaZr_{0.8}Y_{0.2}O_{3-\delta}$	Combustion	1600/6	550/wet H_2 (~3% H_2O) 600/wet H_2 (~3% H_2O) 650/wet H_2 (~3% H_2O)	9.4×10^{-4} 1.28×10^{-3} 1.78×10^{-3}	[131]
$BaZr_{0.8}Y_{0.2}O_{3-\delta}$	SSRS	1500/10	600/wet air 600/dry air 600/wet H_2 600/dry H_2	6.94×10^{-3} 6.13×10^{-3} 3.40×10^{-3} 6.19×10^{-4}	[108]
$BaZr_{0.8}Gd_{0.16}Zn_{0.04}O_{3-\delta}$ $BaZr_{0.8}Gd_{0.14}Zn_{0.06}O_{3-\delta}$	Citric acid - EDTA	1500/5	500/wet H_2 (~3% H_2O) 750/wet H_2 (~3% H_2O)	5.17×10^{-6} 2.54×10^{-3}	[132]
$BaZr_{0.9}Y_{0.1}O_{3-\delta}$	Wet-chemical combustion	1500-1600/12	400/humid reducing atmosphere	2.4×10^{-3}	[99]
$BaZr_{0.8}In_{0.2}O_{3-\delta}$	Glycine-nitrate combustion	1600/10	600/wet H_2 (1.9% H_2O)	1.1×10^{-3}	[138]
$BaZr_{0.9}Y_{0.1}O_{3-\delta}$	Sol-gel	1000 or 1200/5	450/H_2 500/H_2 550/H_2	1.91×10^{-1} 2.27×10^{-1} 2.54×10^{-1}	[110]
$BaZr_{0.4}Ce_{0.4}Y_{0.2}O_{3-\delta}$	SSRS	1400/8	600/Ar (10% H_2)	4.2×10^{-3}	[97]
$BaZr_{0.6}Ce_{0.2}Y_{0.2}O_{3-\delta}$		1400/12		5.2×10^{-3}	
$BaZr_{0.7}Ce_{0.1}Y_{0.2}O_{3-\delta}$		–		2.7×10^{-3}	
$BaZr_{0.8}Y_{0.2}O_{3-\delta}$		–		2.2×10^{-3}	
$BaCe_{0.9}Zr_0Y_{0.1}O_{2.95}$ $BaCe_{0.2}Zr_{0.7}Y_{0.1}O_{2.95}$	SSRS	1700/6	500/moist air (p_{H_2O}= 0.023 atm)	8×10^{-2} 8×10^{-3}	[106]
$BaZr_{0.75}Ce_{0.05}Y_{0.2}O_{3-\delta}$	SSRS	1550	550/Ar (3% H_2O, 10% H_2) 500/Ar (3% H_2O, 10% H_2) 550/Ar (3% H_2O, 10% H_2)	1.6×10^{-3} 2.9×10^{-3} 3.1×10^{-3}	[139]
$BaZr_{0.7}Ce_{0.2}Y_{0.1}O_{3-\delta}$	SSRS	1550/0.8	600/Ar (3% wet H_2)	2.58×10^{-4}	[140]
$BaZr_{0.5}Ce_{0.3}Y_{0.2}O_{3-\delta}$ + NiO (before calcination)	Solid-state reaction	1600/10	600/dry air 600/wet N_2 600/wet H_2	3.4×10^{-3} 1.38×10^{-2} 4.46×10^{-2}	[92]
$BaZr_{0.5}Ce_{0.3}Y_{0.2}O_{3-\delta}$		1600/24	600/dry air	5.0×10^{-4}	

(*continued on next page*)

Table 5 (*continued*)

Electrolyte materials	Synthesis method	Sintering temperature (°C)/ time (h)	T (°C)/atmosphere	Total conductivity, σ (S cm^{-1})	Ref.
$BaZr_{0.5}Ce_{0.3}Y_{0.2}O_{3-\delta}$ + NiO (after calcination)		1600/10	600/wet N_2	1.1×10^{-3}	
			600/wet H_2	1.5×10^{-3}	
			600/dry air	9.0×10^{-4}	
			600/wet N_2	1.7×10^{-3}	
			600/wet H_2	4.9×10^{-3}	

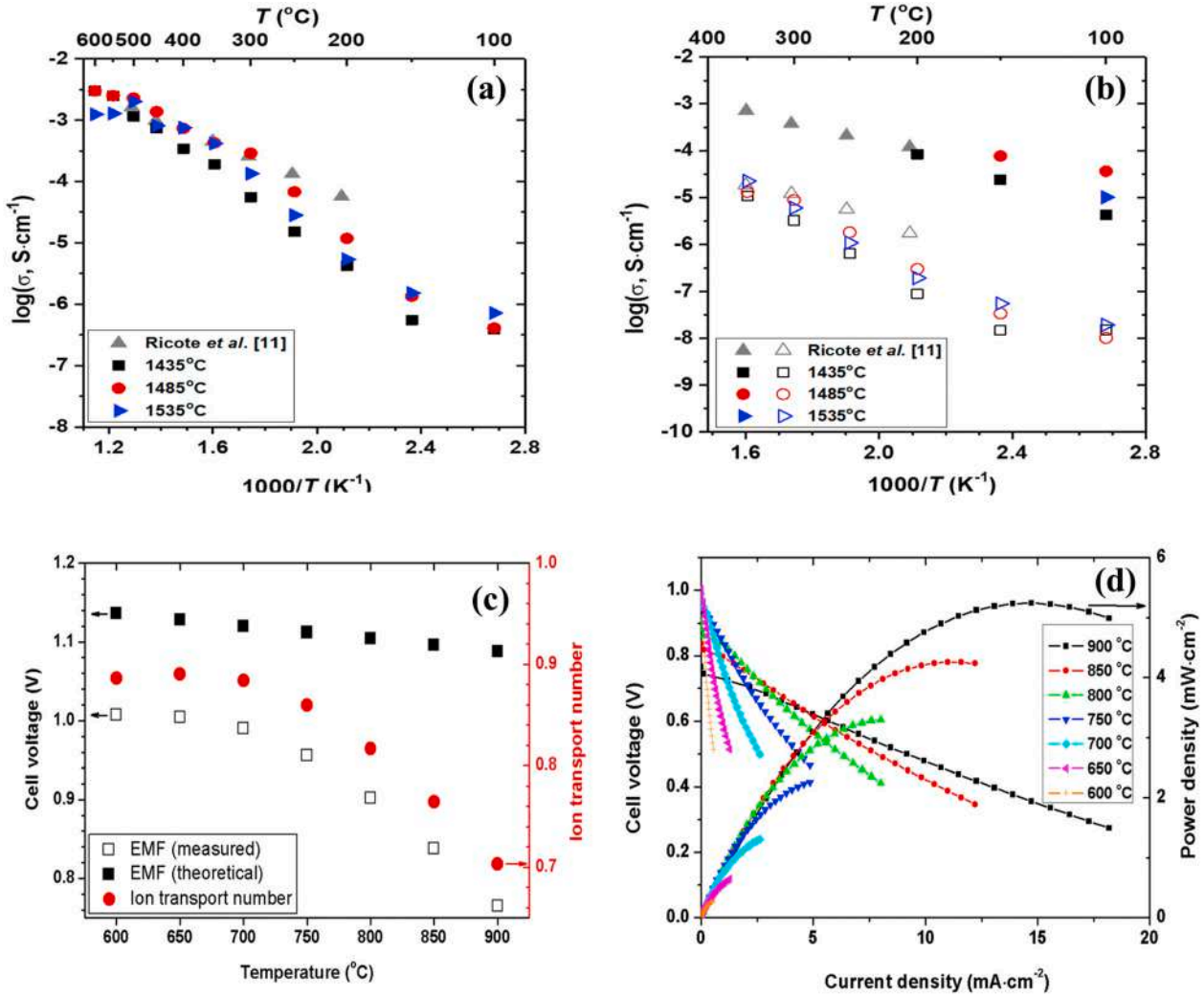

Fig. 12. (a) Arrhenius plot of total proton conductivity and (b) (empty symbols) grain-boundary conductivities and (filled symbols) bulk conductivity of BZY sintered at 1435, 1485, and 1535 °C for 15 h. (c) Measured and theoretical EMF values of Pt/BZY/Pt fuel cell with total ionic transport number (d) power density and current-voltage curves of Pt/BZY/Pt fuel cell at different temperatures [93].

than the similar cell with $BaZr_{0.75}Pr_{0.5}Y_{0.2}O_{3-\delta}$ electrolyte [137]. The performance can be further optimized by cell microstructure and nanoparticle impregnation. So, it is concluded that Gd–Zn co-doping is an effective way and has a great improvement in sinterability, mechanical properties, and conductivity, leading to high electrochemical performance of protons conducting SOFC.

6. Current challenges and prospects

$BaZrO_3$ is the most promising proton conductor electrolyte among all electrolytes as a potential alternative of oxygen conductor due to high proton conductivity and excellent chemical stability at an intermediate operating temperature [156,157]. However, they showed poor sinterability, requiring high sintering temperature (1700–2100 °C) to promote desired microstructure and grain growth, defects due to the dopants and/or sintering aids, negative effects of sintering aids on hydration ability, ionic conductivity and electronic transport number, long-term instability in CO_2, complicated phase compatibility, and so on.

The partial infusion of M dopant into A site instead of B site might lead to defects, e.g., consumption of oxygen vacancies instead of creation, in ABO_3 perovskite lattice structure. Dopants defects significantly lowered the overall proton conduction. It has been observed that A site replacement occurred if the dopant has a higher ionic radius compared to the B site and similar to A site [158–160]. In addition, Ba content depletion from the original composition via BaO vaporization also leads to A site replacement. It is reported A site replacement is prominent due to energetically favorable in $BaCeO_3$ perovskite [161]. A rational dopant selection can lead to defects-free and stable lattice structure [162].

Table 6
Fuel cell performance (peak power density, P_{max}, and open-circuit voltage, OCV) of different electrolyte materials with their ohmic and polarization resistance.

Electrolyte materials	Electrolyte thickness (μm)	Operating temperature (°C)	Ohmic resistance, R_Ω (Ω cm^2)	Polarization resistance, R_p (Ω cm^2)	OCV (V)	P_{max} (mW cm^{-2})	Ref
$BaZr_{0.8}Y_{0.15}Sm_{0.05}O_{3-\delta}$	25	600	1.84	1.4	1.01	92	[95]
		700	1.01	0.18	0.92	180	
$BaZr_{0.75}In_{0.2}Bi_{0.05}O_{3-\delta}$	12	600	0.78	0.41	0.99	180	[129]
		650	0.53	0.29	0.98	260	
		700	0.4	0.18	0.96	340	
$BaZr_{0.8}Y_{0.15}Ca_{0.05}O_{3-\delta}$	15	600	1.63	1.49	1.006	84	[107]
		650	1.11	0.52	0.976	145	
		700	0.76	0.21	0.928	218	
$BaZr_{0.8}Y_{0.2}O_{3-\delta}$	–	350	–	–	1	26.7	[149]
		400	–	–	–	72.4	
$BaZr_{0.8}Y_{0.2}O_{3-\ \delta}$	20	750	4.4	9.8	0.916	24	[150]
$BaZr_{0.8}Y_{0.2}O_{3-\delta}$	~0.08	400	0.085	3.660	1.02	206	[151]
		350	0.099	11.899	–	51	
		375	0.089	7.045	0.425	93	
$BaZr_{0.6}Fe_{0.2}Y_{0.2}O_{3-\delta}$	–	700	–	13.46	0.977	~13	[116]
$BaZr_{0.4}Fe_{0.4}Y_{0.2}O_{3-\ \delta}$			–	2.72	0.979	~53	
$BaZr_{0.2}Fe_{0.6}Y_{0.2}O_{3-\ \delta}$			–	0.287	0.952	~322	
$BaZr_0Fe_{0.8}Y_{0.2}O_{3-\ \delta}$			–	0.15	0.963	~248	
$BaZr_{0.8}Y_{0.2}O_{3-\delta}$	1000	900	–	–	–	~5	[93]
$BaZr_{0.75}Y_{0.2}Pr_{0.05}O_{3-\delta}$	–	500	–	–	0.99	43	[137]
		550	–	–	0.96	70	
		600	1.01	0.4	0.93	124	
$BaZr_{0.8}Y_{0.2}O_{3-\delta}$	23	550	2.45	1.25	1	66	[131]
		600	1.79	0.53	0.96	91	
		650	1.29	0.25	0.9	121	
$BaZr_{0.9}Y_{0.1}O_{3-\delta}$	140	80	–	–	–	0.61	[105]
$BaZr_{0.8}Y_{0.2}O_{3-\ \delta}$	200–400	500	–	–	1.082	~15	[152]
		600	3.8	1.9	1.054	~37	
$BaZr_{0.8}Y_{0.2}O_{3-\delta}$	2000	600	–	–	0.97	–	[108]
$BaZr_{0.8}Y_{0.2}O_{3-\delta}$	20	550	–	–	–	187	[103]
		600	0.44	0.26	0.99	267	
		650	–	–	–	327	
$BaZr_{0.8}Y_{0.2}O_{3-\delta}$	1500	650	–	–	0.88	340	[96]
$BaZr_{0.8}Gd_{0.2}O_{3-\delta}$			–	–	0.9	240	
$BaZr_{0.8}Sm_{0.2}O_{3-\delta}$			–	–	0.89	320	
$BaZr_{0.8}Gd_{0.16}Zn_{0.04}O_{3-\delta}$	30	550	–	–	1.01	37	[132]
		600	–	–	1	63	
		650	–	–	0.98	141	
		700	–	–	0.93	282	
$BaZr_{0.9}Y_{0.1}O_{3-\delta}$	1000	–	–	–	–	–	[99]
$BaZr_{0.8}Y_{0.2}O_{3-\delta}$	20	500	–	–	0.78	156	[145]
$BaZr_{0.8}In_{0.2}O_{3-\ \delta}$	10	600	0.91	0.49	1.01	143	[138]
$BaZr_{0.8}Y_{0.2}O_{3-\ \delta}$	15	550	–	~4.9		44	[153]
(with blank LCSF cathode)		600	–	2.17	–	~70	
		650	–	~0.09	–	166	
		700	–	~0.02	–	~210	
$BaZr_{0.8}Y_{0.2}O_{3-\ \delta}$	15	550	–	~1.5	–	132	
(with impregnated LCSF cathode)		600	–	0.58	–	198	
		650	–	~0.02	–	262	
		700	–	~0.01	–	~320	
$BaZr_{0.9}Y_{0.1}O_{3-\delta}$	500	450	0.12	0.79	–	~326	[110]
		500	0.1	0.35	–	~538	
		550	0.09	0.27	–	~736	
$BaZr_{0.4}Ce_{0.4}Y_{0.2}O_{3-\ \delta}$	30	550	–	–	–	205	[97]
		600	1.41	–	1.07	279	
	30	650	–	–	–	340	
		700	–	–	–	381	
$BaZr_{0.6}Ce_{0.2}Y_{0.2}O_{3-\delta}$	30	550	–	–	–	264	
		600	1.72	–	1.08	336	
		650	–	–	–	396	
		700	–	–	–	435	
$BaZr_{0.7}Ce_{0.1}Y_{0.2}O_{3-\delta}$	30	600	0.75	–	1.05	111	
$BaZr_{0.8}Y_{0.2}O_{3-\delta}$	30	600	0.76	–	0.93	102	
($BaZr_{0.8}Y_{0.2}O_{3-\delta}$) - ($BaCe_{0.8}Y_{0.2}O_{3-\delta}$)	20	600	~0.95	~3.7	0.98	51	[144]
		650	~0.7	~2.05	0.97	81	
		700	~0.65	~1.1	0.96	131	
$BaZrO_3$	15	500	–	–	–	249	[154]
		550	–	–	–	389	
		600	~0.23	0.08		602	
$BaZr_{0.85}Y_{0.15}O_{3-\ \delta}$	2.5	450	–	–	–	342	[91]
		500	–	–	–	457	
		550	–	–	–	563	

(continued on next page)

Table 6 (*continued*)

Electrolyte materials	Electrolyte thickness (μm)	Operating temperature (°C)	Ohmic resistance, R_Ω (Ω cm^2)	Polarization resistance, R_p (Ω cm^2)	OCV (V)	P_{max} (mW cm^{-2})	Ref
		600	–	–	1.0	740	
$BaZr_{0.9}Y_{0.1}O_{2.95}$ $BaCe_{0.2}Zr_{0.7}Y_{0.1}O_{2.95}$	0.065 ± 0.01	500	–	–	–	–	[106]
$BaZr_{0.53}In_{0.47}O_{3-\delta}$ (hydrated structure)	50	300	–	–	–	–	[112]
$BaZr_{0.8}Y_{0.2}O_{3-\delta}$	20	500	0.63	3.32	–	109	[155]
		550	0.5	1.36	–	154	
		600	0.41	0.64	–	200	

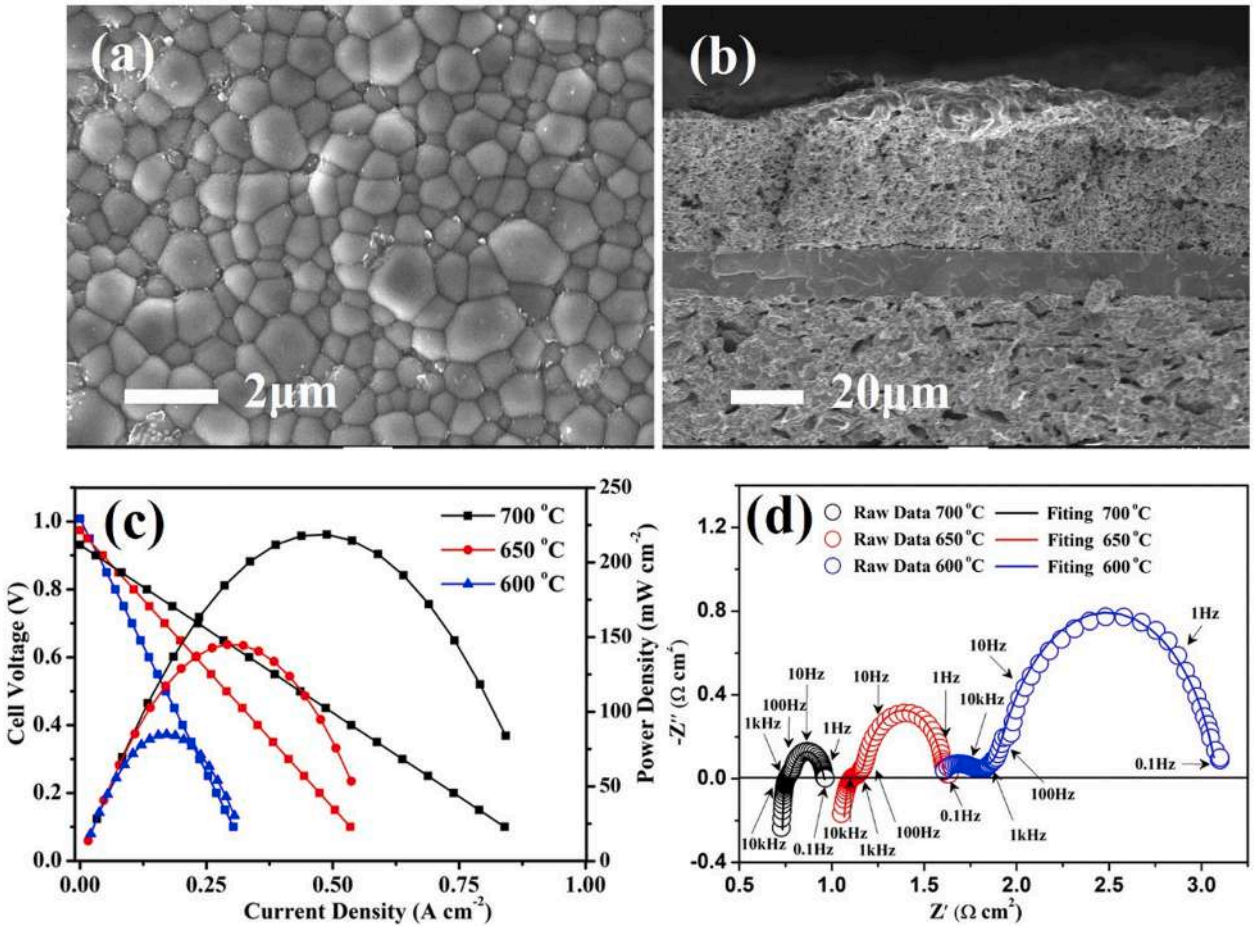

Fig. 13. (a) Surface morphology (SEM micrograph) of the $BaZr_{0.8}Y_{0.15}Ca_{0.05}O_{3-\delta}$ (BZYC5) electrolyte film, (b) single cell's cross-sectional SEM micrograph, (c) single cell's I–V and I–P characteristics curves, (d) single cell's electrochemical impedance spectroscopy (EIS) measurement results in open-circuit voltage (OCV) condition at three different temperatures, 600 °C, 650 °C, and 700 °C [107].

Other defects due to dopants infusion with potentially higher ionic radius than B site is lattice distortion [161,163]. The higher dopant concentration or larger size leads to unit cell volume variation, resulting in strain induced in the system. This implies the overall distortion in the structure and reduces the proton conductivity of the high-temperature proton conductors [161,164]. These results suggest the choice of dopant with a similar ionic radius of B site and stable oxidation state of +2 is favorable for stable lattice structure of ABO_3- type perovskites.

In addition, long term sintering step (>24 h) also restricts their promising applications. This processing condition not only raises the production cost and process incompatibilities but also significantly reduces the proton conductivity via barium vaporization and yttria formation (in the case of Y-doped $BaZrO_3$) during sintering [99]. This can be ascribed due to reduced occupancy of A sites in the microstructure allowing dopant substitution and thereby lower concentration of oxygen vacancies. Babilo et al. observed that covering of BZY20 during sintering significantly reduces BaO loss results in a 3-fold conductivity enhancement compared to the uncovered sample at 100 °C [165].

Researchers overcame the low sinterability of BZY with the addition of small amounts of sintering aids such as ZnO, NiO, CuO, SnO, BaO, MgO, and Al_2O_3 [166–168]. The prime objective of the inclusion of these additives is to reduce sintering temperature to intermediate operating condition temperature so that the fabricated BZY can be applied to classical intermediate temperature solid oxide fuel cell

(IT-SOFC) cell fabrication methods. An ideal sintering additive (e.g., metal ions) should possess a stable oxidation state of +2 and ionic radium close to Zr^{4+} in order to reside in the $BaZrO_3$ structure and generates a large percentage of defects [166–168]. There is also a possibility that metal ions having multiple oxidation states can take part as sintering aids. A rational selection of metal ions and structure design is needed to achieve high sinterability and conductivity.

Among the aforementioned additives, Zn showed the excellent potential to reduce sintering temperature. Research conducted by P. Babilo and S. M. Haile at CalTech showed that the addition of ZnO significantly improved the sinterability and chemical stability of BZY at 1300 °C [112]. Among all the transition metal elements from Sc to Zn, the high densification efficiency of ZnO at 4 mol% and 1300 °C was observed. However, the conductivity of ZnO infused BZY was found lower compared to unmodified BZY despite the uniform distribution of ZnO at grain boundaries, high chemical stability, and homogeneous grain size. The reason behind this is the potential proton trapping at Zn''_{Zr} sites. Unfortunately, no evidence was found as it is way below the detection limit of EDS analysis.

Similar research observed that at 1 wt% ZnO addition, the sintering temperature of 20 mol% Y-doped $BaZrO_3$ significantly reduced from 1700 °C to 1300 °C [168]. The authors found that the fabricated $Ba_{0.97}Zr_{0.77}Y_{0.19}Zn_{0.04}O_{3-\delta}$ is highly dense, single-phase, and exhibited a tetragonal structure, which eventually enhances the proton conduction at a much lower temperature. The high grain boundary surface area dominated poor proton conduction at a lower temperature, whereas ZnO induced BZY showed a total conductivity of 1.0×10^{-3} Scm^{-1} at above 600 °C, which widens its application in intermediate temperature electrochemical devices [168]. Another experiment investigated the sinterability of BZY with the aid of a novel composition of BaO–CuO mixture at a ratio of 28 mot% and 72 mol%, respectively [169]. M. Biswas et al. observed that the eutectic mixture of BaO–CuO significantly improved the sinterability and formed dense as high as 97% nanocrystalline BZY powder [169]. With the aid of a eutectic flux, the pinning mechanism can be avoided, which is deleterious for grain growth. Other advantages of binary flux are including but not limited to particle rearrangement and suppressing surface diffusion at intermediate temperatures. With the increased temperature, grain growth dominates and forms an extremely dense solid [170,171]. Previously reported results showed that single phase inclusion of 1 wt% CuO as sintering aid offers only 3% shrinkage at 1200 °C, whereas, BaO–CuO flux showed as high as 18.5% shrinkage at the same conditions [169].

A new concept of reactive sintering, consisting of solid-state synthesis and reactive sintering, termed as "solid-state reactive sintering" (SSRS), exhibited the great potential of synthesis single-phase, highly dense, and well-developed grain growth in a single step sintering approach. This method not only reduced sintering temperature by 200–400 °C compared to traditional processes and production costs by 10-fold but also overcame various challenges linked with $BaZrO_3$-based perovskite [172]. Though researchers have a great understanding of the benefits of the SSRS method, there is an extensive dearth of literature regarding the general mechanism of the SSRS method. Recently, Nikodemski et al. investigated the mechanism of the SSRS method in a prototypical perovskite $BaCe_{0.6}Zr_{0.3}Y_{0.1}O_{3-\delta}$ ($BCZY6_3$) via analyzing the microstructure development due to the infusion of metal ions as sintering additives [94]. The results showed that metal ions had a 2^+ oxidation state, and similar radii of Zr^{4+} greatly improved sinterability and conductivity. The proposed SSRS mechanism is shown in Fig. 14, which visually depicts the influence of dopants and sintering aids, allows to rationalize materials selection in order to obtain any desired morphology of BZY perovskites.

As high grain boundary surface area is detrimental to proton conductivity, it is in great interest to obtain high grain size. $BaZrO_3$ exhibits lower grain boundary conductivity compared to $BaCeO_3$ due to its high grain boundary resistance. Some works were conducted to explain this phenomenon by the space charge layer model. J.M. Polfus et al. observed the positive charge layer formation through accumulation at the surface that resembles the space charge layer formation on the grain boundary [173]. L.P. Wendler et al. investigated the poor grain growth of Y-doped $BaZrO_3$ via analyzing the microstructure [156]. During sintering, the formation of BZ microstructure was developed at 1100 °C. With the increasing temperature, the BZ phase transition towards BZY occurred at 1600 °C with the inclusion of Y^{3+} in the final structure. A formation of an yttria-like secondary phase at around 1500 °C was found, which acts as pinning and restricts grain growth. Therefore, to trigger the growth of grain boundary and inhibit secondary phase formation during sintering, it is required to avoid yttria phase formation. This might be done by lowing the Y content or using alternative dopants.

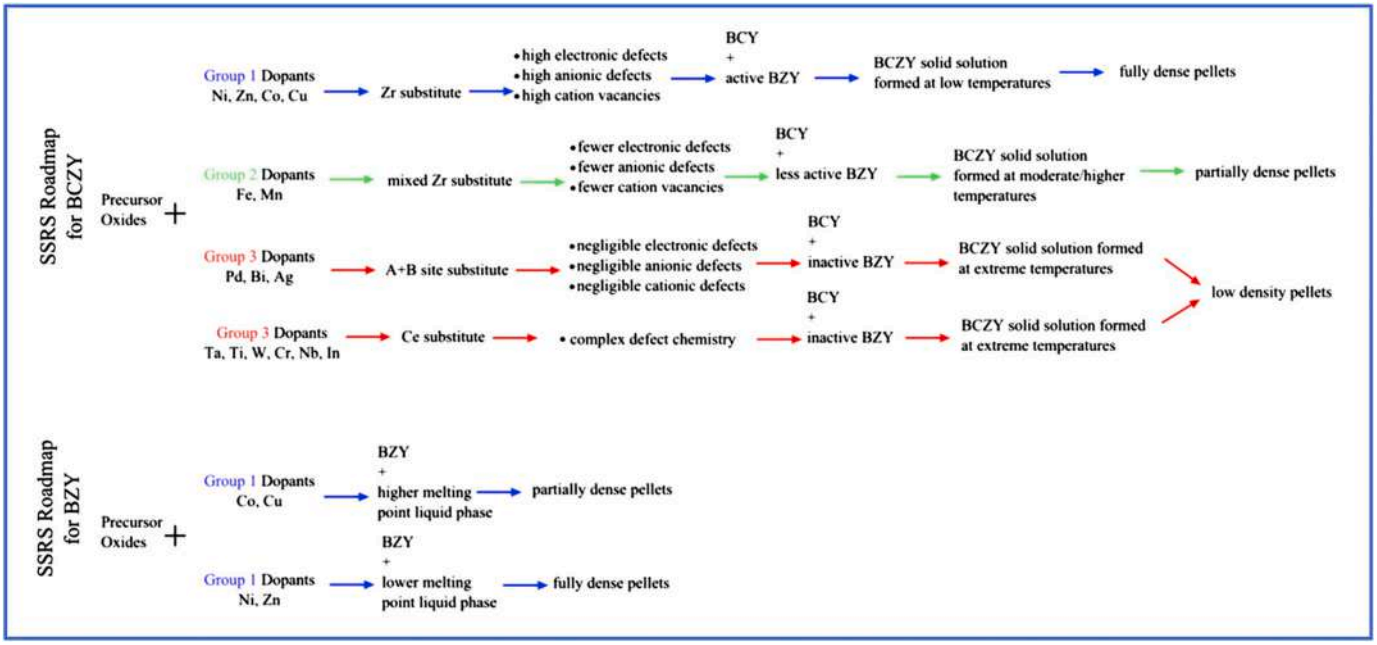

Fig. 14. Solid-state reactive sintering (SSRS) roadmap [94].

Although sintering aids showed excellent performance to enhance sinterability and grain growth, these additives might cause inevitable deleterious effects on the electrical conductivity of BZY perovskites. The co-sintering approach carried out at 1500 °C, commonly used as a cell fabrication method, has a negative effect on the performance of electrochemical devices. The reasons are the poor phase compatibility of BZY and metal oxide system, secondary phase formation, and reduction of ionic conduction. An experiment conducted by D. Han et al. on the influence of sintering additives on BZY20 and found that the transport number of ionic conductions at 600 °C significantly reduced from 0.69 to 0.34, 0.39, and 0.43 at 2 wt% NiO, CuO, and ZnO infusion respectively into BZY20 sample compared to pure BZY [174]. In addition, the self-diffusion of NiO from anode to the BZY electrolyte layer took part to reduce the conductivity as well. The reduced proton concentration with increasing Ni concentration was observed during hydration reaction, equates to lower oxide ion vacancies (V_O), and promotes electron-hole (h) formation by the following reactions.

$$H_2O + V_o^{\bullet\bullet} + O_o^{\times} = 2OH_o^{\bullet} \quad (7)$$

$$O_2 + 2V_o^{\bullet\bullet} \leftrightarrow 2O_o^{\times} + 4h^{\bullet} \quad (8)$$

Therefore, the utilization of sintering aids or their removal after sintering via post-annealing is in great interest to avoid their detrimental effects on proton conduction [174]. D. Han et al. proposed a post-annealing approach at reduced temperature (700 °C) [174]. The data revealed the favorable removal of Cu and Ni at hydrogen atmosphere at desired temperature both from intragrain and grain boundary areas. However, the complete removal of sintering aids at lower temperatures requires a longer soaking/sintering step or higher temperature, for instance, 1400 °C. In another paper from the same group, Yb was used as a dopant instead of Y to enhance the phase compatibility between BZY and NiO as well as to suppress the formation of secondary phases [175]. In this instance, excellent phase compatibility between $BaZrO_3$-based electrolyte ($BaZr_{0.8}Yb_{0.2}O_{3-\delta}$) (BZYb20) and NiO electrode substrate. This can be ascribed due to the uniform distribution of the components in the electrolyte layer. Their study also revealed the suppression of secondary phase formation at lower Y content in $BaZr_{1-x}Y_xO_{3-\delta}$ (BZY) where x = 0.12. However, evidence of Ni diffusion during this high temperature co-sintering process was observed. It is also reported in the literature that in case of In doped BZY, $BaZr_{0.8}In_{0.2}O_{3-\delta}$ (BZIn20) showed better compatibility with NiO but exhibited poor proton conductivity [176]. Therefore, it is worth mentioning that these issues cannot be easily overcome by reducing doping levels or changing dopants. So, it is greatly in need to develop new sintering additives, anode catalysts, and cell fabrication techniques.

In addition, mechanical stability also plays a vital role in restricting the broad application of BZY perovskite-based electrolytes with sintering issues and less dense structure. To reduce the ohmic resistance of the BZY film, it greatly depends on the film thickness. The reduced film thickness of BZY electrolytes exhibited significantly lowered ohmic resistance and higher conductivity [91]. This can be attributed that high grain boundaries induced high ohmic resistance and less power output [177,178]. Therefore, grain boundary elimination and/or reduction during BZY electrolyte fabrication is the key to enhance the proton conduction [179]. Developing thin-film BZY electrolytes while reducing or eliminating grain boundaries may cause poor mechanical stability of the free-standing membrane electrode assemblies (MEAs). Hence, the key challenge of improving the proton conductivity of thin and dense BZY membrane is to maintain structural integrity and mechanical stability. However, some recent studies reported that highly dense thick films are promising materials for SOFCs due to high ionic conductivity. A group of researchers fabricated highly dense films of barium-based perovskite ceramics, namely barium zirconates ($BaZrO_3$), barium stannates ($BaSnO_3$), and barium cerates ($BaCeO_3$), via a novel method Powder Aerosol Deposition (PAD) [180]. This is a spray coating approach where the films were formed at room temperature without sintering. They found that the adhesion between dense solid electrolyte (e.g., BCY20/BZY20) and porous anode (NiO) could be improved by the PAD technique which eventually improved the phase compatibility, film thickness, structural integrity, stability, and ionic conductivity.

It is important to keep in mind that the materials selection criteria principally depend on the operation temperature of individual electrochemical devices. For example, operation temperature in the range of 800–1000 °C is ideal for a proton conducting membranes for hydrogen separation [181,182]. Where, SOFC devices, it principally in the range of 400–600 °C for intermediate proton conducting oxide as electrolyte materials [183–185]. Keeping such considerations, $BaCeO_3$ (BCO) and $BaZrO_3$ (BZO) are the two main proton conducting oxides that dominates the most recent research activities. $SrCeO_3$ is another proton conducting oxides that has small traction too. BCO provides better proton conductivity among all these materials, however, due to the basicity of BCO, it easily reacts with acidic gases (CO_2 and SO_2) and H_2O and hence has poor chemical stability. The interesting trend is that although all of them have different material drawbacks to overcome, however, doping seems to be a common technique to overcome these drawbacks. Doping with Yttrium was found to be most effective to improve the conductivity of BCO. Other metals such as Sc, Ta, Tb, Gd, In, etc. were used as dopants to improve the material stability of BCO [182,183,186]. Among those dopants, Sc^{3+} is reported to provide the best chemical stability due to the small atomic size in the trivalent rare earth group [186].

It is well-known that BCO provides the best proton conductivity and BZO has better chemical stability among the proton conducting oxides. Therefore, a recent trend is to combine these two perovskite oxides to optimize the better properties [184,185]. The choice between incorporating Zr into BCO or Ce into BZO depends on the final objective. Like, incorporation of Ce into $BaZrO_3$ improves the overall conductivity, sinterability, however, decreases its chemical stability in CO_2 and water vapor conditions. Apart from the final composite chemical composition, the synthesis routes play a key role. The solid-state reaction method was reported to produce better performing such composites compare to the wet chemical, citrate combustion method [187]. One important thing to be noted that doping with rare earth metal with mixed BZO-BCO composites results in improved properties. Therefore, the opportunity to optimize materials is still going at a rapid speed.

7. Conclusions

The depletion of fossil fuels, global awareness of environmental issues and growing demand for clean energy forced the scientific community to search for green alternatives. The electrochemical hydrogen devices like fuel cells showed excellent potential as clean and renewable energy sources. These devices require highly stable and higher conductive electrolytes, especially at the intermediate temperature range, in which perovskite oxides are prominent. Among various perovskites, $BaZrO_3$ exhibited tremendous performance as solid ion-conducting perovskite material at a temperature range of 400–650 °C after modifications in fabrication techniques, which include doping and co-doping, adding sintering aids, and so on. The inclusion of metallic and non-metallic dopants with different ionic radii and electronegativity allows achieving high stability and superior proton conductivity of perovskites. However, based on the experimental data, it has been observed that dopants' size and concentration lead to unit cell volume expansion, results in strain induction, distortion, and overall reduce proton conductivity. To overcome these inconsistencies, various investigations on $BaZrO_3$ are highlighted in this review, which includes co-doing, dopant with similar ionic radii of B site, and stable oxidation state. In addition, high sintering temperature and long-term sintering

step associated with various synthesis methods restrict their wide applications and commercialization. Researchers overcame the low sinterability of BZY with the addition of small amounts of sintering aids for the practical applications of this electrolyte at intermediate operating temperature conditions. Solid-state reactive sintering (SSRS) showed the excellent performance to synthesize single-phase, highly dense, and well-developed grain growth in a single-step sintering approach by decreasing sintering temperature by 200–400 °C compared to traditional processes and production cost by 10-fold. This is worth mentioning that all the strategies and modifications carried out with the increase of electrolytes' conductivity and sinterability, a reduction in structural integrity, mechanical stability, and ionic and protonic conductivity occurs to a greater or lesser extent, which still restricts their practical applications and adoption by industry. Therefore, scientists are studying materials that would be thermodynamically stable and highly suitable for proton-conducting at intermediate temperatures that might be ideal electrolyte materials for electrochemical hydrogen devices.

Declaration of competing interest

The authors declare that they have no known competing financial interests or personal relationships that could have appeared to influence the work reported in this paper.

Acknowledgment

Taif University Researchers Supporting Project number (TURSP-2020/45) Taif University, Taif, Saudi Arabia.

References

[1] N. Sazali, Emerging technologies by hydrogen: a review, Int. J. Hydrogen Energy 45 (2020) 18753–18771, https://doi.org/10.1016/j.ijhydene.2020.05.021.
[2] C. Duan, J. Huang, N. Sullivan, R. O'Hayre, Proton-conducting oxides for energy conversion and storage, Appl. Phys. Rev. 7 (2020), 011314, https://doi.org/10.1063/1.5135319.
[3] H. Iwahara, Hydrogen pumps using proton-conducting ceramics and their applications, Solid State Ionics 125 (1999) 271–278, https://doi.org/10.1016/S0167-2738(99)00185-X.
[4] P. Pasierb, M. Rekas, High-temperature electrochemical hydrogen pumps and separators, Int. J. Electrochem. 2011 (2011) 1–10, https://doi.org/10.4061/2011/905901.
[5] C. Athanassiou, G. Pekridis, N. Kaklidis, K. Kalimeri, S. Vartzoka, G. Marnellos, Hydrogen production in solid electrolyte membrane reactors (SEMRs), Int. J. Hydrogen Energy 32 (2007) 38–54, https://doi.org/10.1016/j.ijhydene.2006.06.031.
[6] C. Duan, J. Tong, M. Shang, S. Nikodemski, M. Sanders, S. Ricote, A. Almansoori, R. OHayre, Readily processed protonic ceramic fuel cells with high performance at low temperatures, Science 349 (2015) 1321–1326, https://doi.org/10.1126/science.aab3987.
[7] M.K. Hossain, M.C. Biswas, R.K. Chanda, M.H.K. Rubel, M.I. Khan, K. Hashizume, A review on experimental and theoretical studies of perovskite barium zirconate proton conductors, Emergent Mater (2021), https://doi.org/10.1007/s42247-021-00230-5.
[8] D.G. Thomas, J.J. Lander, Hydrogen as a donor in zinc oxide, J. Chem. Phys. 25 (1956) 1136–1142, https://doi.org/10.1063/1.1743165.
[9] J.M. Pope, G. Simkovich, The use of $BaTiO_3$ as a solid-electrolyte to determine water vapor effects upon electrical transport mechanisms, Mater. Res. Bull. 9 (1974) 1111–1117, https://doi.org/10.1016/0025-5408(74)90026-9.
[10] H. Iwahara, H. Uchida, N. Maeda, High temperature fuel and steam electrolysis cells using proton conductive solid electrolytes, J. Power Sources 7 (1982) 293–301, https://doi.org/10.1016/0378-7753(82)80018-9.
[11] H. Iwahara, H. Uchida, S. Tanaka, High temperature-type proton conductive solid oxide fuel cells using various fuels, J. Appl. Electrochem. 16 (1986) 663–668, https://doi.org/10.1007/BF01006916.
[12] K.D. Kreuer, Proton-conducting oxides, Annu. Rev. Mater. Res. 33 (2003) 333–359, https://doi.org/10.1146/annurev.matsci.33.022802.091825.
[13] K.D. Kreuer, S. Adams, W. Münch, A. Fuchs, U. Klock, J. Maier, Proton conducting alkaline earth zirconates and titanates for high drain electrochemical applications, Solid State Ionics 145 (2001) 295–306, https://doi.org/10.1016/S0167-2738(01)00953-5.
[14] E. Fabbri, L. Bi, D. Pergolesi, E. Traversa, Towards the next generation of solid oxide fuel cells operating below 600 °C with chemically stable proton-conducting electrolytes, Adv. Mater. 24 (2012) 195–208, https://doi.org/10.1002/adma.201103102.
[15] B.C.H. Steele, A. Heinzel, Materials for fuel-cell technologies, Nature 414 (2001) 345–352, https://doi.org/10.1038/35104620.
[16] Z. Hui, P. Michèle, Preparation, chemical stability, and electrical properties of $Ba(Ce_{1-x}Bi_x)O_3$ (x = 0.0–0.5), J. Mater. Chem. 12 (2002) 3787–3791, https://doi.org/10.1039/B205107A.
[17] C.W. Tanner, A.V. Virkar, Instability of $BaCeO_3$ in H_2O -containing atmospheres, J. Electrochem. Soc. 143 (2019) 1386–1389, https://doi.org/10.1149/1.1836647.
[18] H. Borland, L. Llivina, S. Colominas, J. Abellà, Proton conducting ceramics for potentiometric hydrogen sensors for molten metals, Fusion Eng. Des. 88 (2013) 2431–2435, https://doi.org/10.1016/j.fusengdes.2013.05.055.
[19] M. Tanaka, T. Ohshima, Recovery of hydrogen from gas mixture by an intermediate-temperature type proton conductor, Fusion Eng. Des. 85 (2010) 1038–1043, https://doi.org/10.1016/j.fusengdes.2010.01.007.
[20] D. Gao, R. Guo, Structural and electrochemical properties of yttrium-doped barium zirconate by addition of CuO, J. Alloys Compd. 493 (2010) 288–293, https://doi.org/10.1016/j.jallcom.2009.12.082.
[21] H. Bae, Y. Lee, K.J. Kim, G.M. Choi, Effects of fabrication conditions on the crystallinity, barium deficiency, and conductivity of $BaZr_{0.8}Y_{0.2}O_{3-\delta}$ films grown by pulsed laser deposition, Fuel Cell. 15 (2015) 408–415, https://doi.org/10.1002/fuce.201400004.
[22] J. Tong, D. Clark, M. Hoban, R. O'Hayre, Cost-effective solid-state reactive sintering method for high conductivity proton conducting yttrium-doped barium zirconium ceramics, Solid State Ionics 181 (2010) 496–503, https://doi.org/10.1016/j.ssi.2010.02.008.
[23] L. Bi, E. Fabbri, Z. Sun, E. Traversa, Sinteractivity, proton conductivity and chemical stability of $BaZr_{0.7}In_{0.3}O_{3-\delta}$ for solid oxide fuel cells (SOFCs), Solid State Ionics 196 (2011) 59–64, https://doi.org/10.1016/j.ssi.2011.06.014.
[24] M.K. Hossain, K. Hashizume, Preparation and characterization of yttrium doped barium-zirconates at high temperature sintering. Proceeding Int. Exch. Innov. Conf. Eng. Sci., IGSES, Kyushu University, Fukuoka, Japan, 2019, pp. 70–72, https://doi.org/10.15017/2552940.
[25] M.K. Hossain, K. Hashizume, Dissolution and release behavior of hydrogen isotopes from barium-zirconates, Proc. Int. Exch. Innov. Conf. Eng. Sci. 6 (2020) 34–39, https://doi.org/10.5109/4102460.
[26] T. Norby, Solid-state protonic conductors: principles, properties, progress and prospects, Solid State Ionics 125 (1999) 1–11, https://doi.org/10.1016/S0167-2738(99)00152-6.
[27] J. Chen, S. Wu, F. Zhang, S. Lü, Y. Mao, Calcination temperature dependence of synthesis process and hydrogen sensing properties of In-doped $CaZrO_3$, Mater. Chem. Phys. 172 (2016) 87–97, https://doi.org/10.1016/j.matchemphys.2015.12.064.
[28] T. Yajima, H. Iwahara, K. Koide, K. Yamamoto, $CaZrO_3$-type hydrogen and steam sensors: trial fabrication and their characteristics, Sensor. Actuator. B Chem. 5 (1991) 145–147, https://doi.org/10.1016/0925-4005(91)80235-C.
[29] H. Matsumoto, Hydrogen isotope cell and its application to hydrogen isotope sensing, Solid State Ionics 136–137 (2000) 173–177, https://doi.org/10.1016/S0167-2738(00)00308-8.
[30] L. Dai, L. Wang, G. Shao, Y. Li, A novel amperometric hydrogen sensor based on nano-structured ZnO sensing electrode and $CaZr_{0.9}In0.1O_{3-\delta}$ electrolyte, Sensor. Actuator. B Chem. 173 (2012) 85–92, https://doi.org/10.1016/j.snb.2012.06.012.
[31] Y. Okuyama, S. Nagamine, A. Nakajima, G. Sakai, N. Matsunaga, F. Takahashi, K. Kimata, T. Oshima, K. Tsuneyoshi, Proton-conducting oxide with redox protonation and its application to a hydrogen sensor with a self-standard electrode, RSC Adv. 6 (2016) 34019–34026, https://doi.org/10.1039/C5RA23560J.
[32] A.S. Kalyakin, J.G. Lyagaeva, A.Y. Chuikin, A.N. Volkov, D.A. Medvedev, A high-temperature electrochemical sensor based on $CaZr_{0.95}Sc_{0.05}O_{3-\delta}$ for humidity analysis in oxidation atmospheres, J. Solid State Electrochem. 23 (2019) 73–79, https://doi.org/10.1007/s10008-018-4108-7.
[33] N. Taniguchi, T. Kuroha, C. Nishimura, K. Iijima, Characteristics of novel $BaZr_{0.4}Ce_{0.4}In_{0.2}O_3$ proton conducting ceramics and their application to hydrogen sensors, Solid State Ionics 176 (2005) 2979–2983, https://doi.org/10.1016/j.ssi.2005.09.035.
[34] T. Schneller, T. Schober, Chemical solution deposition prepared dense proton conducting Y-doped $BaZrO_3$ thin films for SOFC and sensor devices, Solid State Ionics 164 (2003) 131–136, https://doi.org/10.1016/S0167-2738(03)00308-4.
[35] M. Tanaka, K. Katahira, Y. Asakura, T. Ohshima, Hydrogen pump using a high-temperature proton conductor for nuclear fusion engineering applications, Solid State Ionics 181 (2010) 215–218, https://doi.org/10.1016/j.ssi.2009.01.020.
[36] Y. Kawamura, S. Konishi, M. Nishi, T. Kakuta, Transport properties of hydrogen isotope gas mixture through ceramic protonic conductor, Fusion Sci. Technol. 41 (2002) 1035–1039, https://doi.org/10.13182/FST02-A22741.
[37] Y. Kawamura, S. Konishi, M. Nishi, Extraction of hydrogen from water vapor by hydrogen pump using ceramic protonic conductor, Fusion Sci. Technol. 45 (2004) 33–40, https://doi.org/10.13182/FST04-A423.
[38] A. Ciampichetti, F.S. Nitti, A. Aiello, I. Ricapito, K. Liger, D. Demange, L. Sedano, C. Moreno, M. Succi, Conceptual design of tritium extraction system for the European HCPB test blanket module, Fusion Eng. Des. 87 (2012) 620–624, https://doi.org/10.1016/j.fusengdes.2012.01.047.

[39] H. Iwahara, Study on proton conductive solid electrolyte-recent trends, Electrochemistry 69 (2001) 788–793, https://doi.org/10.5796/electrochemistry.69.788.

[40] O. Antoine, C. Hatchwell, G.C. Mather, A.J. McEvoy, Structure and conductivity of a Yb-doped $SrCeO_3$-$BaZrO_3$ solid solution, ECS Proc 7 (2003) 379–387, https://doi.org/10.1149/200307.0379PV, 2003.

[41] Y. Kawamura, T. Yamanishi, Tritium recovery from blanket sweep gas via ceramic proton conductor membrane, Fusion Eng. Des. 86 (2011) 2160–2163, https://doi.org/10.1016/j.fusengdes.2010.12.003.

[42] T. Chikada, T. Tanaka, K. Yuyama, Y. Uemura, S. Sakurada, H. Fujita, X.-C. Li, K. Isobe, T. Hayashi, Y. Oya, Crystallization and deuterium permeation behaviors of yttrium oxide coating prepared by metal organic decomposition, Nucl. Mater. Energy. 9 (2016) 529–534, https://doi.org/10.1016/j.nme.2016.06.009.

[43] Y. Kawamura, K. Isobe, T. Yamanishi, Mass transfer process of hydrogen via ceramic proton conductor membrane of electrochemical hydrogen pump, Fusion Eng. Des. 82 (2007) 113–121, https://doi.org/10.1016/j.fusengdes.2006.07.094.

[44] M.K. Hossain, K. Kawaguchi, K. Hashizume, Conductivity of gadolinium (III) oxide (Gd_2O_3) in hydrogen-containing atmospheres, Proc. Int. Exch. Innov. Conf. Eng. Sci. 6 (2020) 1–6, https://doi.org/10.5109/4102455.

[45] M.K. Hossain, K. Kawaguchi, K. Hashizume, Isotopic effect of proton conductivity in gadolinium sesquioxide, Fusion Eng. Des. 171 (2021) 112555, https://doi.org/10.1016/j.fusengdes.2021.112555.

[46] T. Xia, C. He, H. Yang, W. Zhao, L. Yang, Hydrogen extraction characteristics of high-temperature proton conductor ceramics for hydrogen isotopes purification and recovery, Fusion Eng. Des. 89 (2014) 1500–1504, https://doi.org/10.1016/j.fusengdes.2014.04.078.

[47] S. Choi, T.C. Davenport, S.M. Haile, Protonic ceramic electrochemical cells for hydrogen production and electricity generation: exceptional reversibility, stability, and demonstrated faradaic efficiency, Energy Environ. Sci. 12 (2019) 206–215, https://doi.org/10.1039/C8EE02865F.

[48] C. Duan, R. Kee, H. Zhu, N. Sullivan, L. Zhu, L. Bian, D. Jennings, R. O'Hayre, Highly efficient reversible protonic ceramic electrochemical cells for power generation and fuel production, Nat. Energy. 4 (2019) 230–240, https://doi.org/10.1038/s41560-019-0333-2.

[49] S. Choi, C.J. Kucharczyk, Y. Liang, X. Zhang, I. Takeuchi, H.-I. Ji, S.M. Haile, Exceptional power density and stability at intermediate temperatures in protonic ceramic fuel cells, Nat. Energy. 3 (2018) 202–210, https://doi.org/10.1038/s41560-017-0085-9.

[50] H. An, H.-W. Lee, B.-K. Kim, J.-W. Son, K.J. Yoon, H. Kim, D. Shin, H.-I. Ji, J.-H. Lee, A 5×5 cm^2 protonic ceramic fuel cell with a power density of 1.3 W cm^{-2} at 600 °C, Nat. Energy. 3 (2018) 870–875, https://doi.org/10.1038/s41560-018-0230-0.

[51] R. Mukundan, E.L. Brosha, S.A. Birdsell, A.L. Costello, F.H. Garzon, R.S. Willms, Tritium conductivity and isotope effect in proton-conducting perovskites, J. Electrochem. Soc. 146 (2019) 2184–2187, https://doi.org/10.1149/1.1391911.

[52] M.K. Hossain, K. Hashizume, S. Jo, K. Kawaguchi, Y. Hatano, Hydrogen isotope dissolution and release behavior of rare earth oxides, Fusion Sci. Technol. 76 (2020) 553–566, https://doi.org/10.1080/15361055.2020.1728173.

[53] W. Mao, T. Chikada, A. Suzuki, T. Terai, H. Matsuzaki, Hydrogen isotope dissolution, diffusion, and permeation in Er_2O_3, J. Power Sources 303 (2016) 168–174, https://doi.org/10.1016/j.jpowsour.2015.10.091.

[54] L. Chen, X. Dong, Y. Wang, Y. Xia, Separating hydrogen and oxygen evolution in alkaline water electrolysis using nickel hydroxide, Nat. Commun. 7 (2016) 11741, https://doi.org/10.1038/ncomms11741.

[55] M. David, C. Ocampo-Martínez, R. Sánchez-Peña, Advances in alkaline water electrolyzers: a review, J. Energy Storage. 23 (2019) 392–403, https://doi.org/10.1016/j.est.2019.03.001.

[56] S.W. Boettcher, Oxygen stays put during water oxidation, Nat. Catal. 1 (2018) 814–815, https://doi.org/10.1038/s41929-018-0179-1.

[57] K. Ito, H. Li, Y.M. Hao, Alkaline water electrolysis. https://doi.org/10.1007/978-4-431-56042-5_9, 2016, 137-142.

[58] N. Lakshmi, S. Chandra, Rechargeable solid-state battery using a proton-conducting composite as electrolyte, J. Power Sources 108 (2002) 256–260, https://doi.org/10.1016/S0378-7753(02)00021-6.

[59] Y. Tang, Y. Zhang, W. Li, B. Ma, X. Chen, Rational material design for ultrafast rechargeable lithium-ion batteries, Chem. Soc. Rev. 44 (2015) 5926–5940, https://doi.org/10.1039/C4CS00442F.

[60] M. Li, J. Lu, Z. Chen, K. Amine, 30 Years of lithium-ion batteries, Adv. Mater. 30 (2018) 1800561, https://doi.org/10.1002/adma.201800561.

[61] Z. Ogumi, R. Kostecki, D. Guyomard, M. Inaba, Lithium-ion batteries–the 25th anniversary of commercialization, Interface Mag 25 (2016), https://doi.org/10.1149/2.F04163if, 65–65.

[62] J.-W. Jeon, M.C. Biswas, C.L. Patton, E.K. Wujcik, Water-processable, sprayable $LiFePO_4$/graphene hybrid cathodes for high-power lithium ion batteries, J. Ind. Eng. Chem. 84 (2020) 72–81, https://doi.org/10.1016/j.jiec.2019.12.022.

[63] P. Knauth, M.L. Di Vona (Eds.), Solid State Proton Conductors, John Wiley & Sons, Ltd, Chichester, UK, 2012, https://doi.org/10.1002/9781119962502.

[64] Y. Wu, C. Xia, W. Zhang, X. Yang, Z.Y. Bao, J.J. Li, B. Zhu, Natural hematite for next-generation solid oxide fuel cells, Adv. Funct. Mater. 26 (2016) 938–942, https://doi.org/10.1002/adfm.201503756.

[65] S. Tao, J.T.S. Irvine, A redox-stable efficient anode for solid-oxide fuel cells, Nat. Mater. 2 (2003) 320–323, https://doi.org/10.1038/nmat871.

[66] D. Makovec, Z. Samardzija, D. Kolar, Solid solubility of neodymium in $BaCeO_3$, J. Am. Ceram. Soc. 80 (2005) 3145–3150, https://doi.org/10.1111/j.1151-2916.1997.tb03243.x.

[67] K.J. Kim, B.H. Park, S.J. Kim, Y. Lee, H. Bae, G.M. Choi, Micro solid oxide fuel cell fabricated on porous stainless steel: a new strategy for enhanced thermal cycling ability, Sci. Rep. 6 (2016) 22443, https://doi.org/10.1038/srep22443.

[68] S. Hossain, A.M. Abdalla, S.N.B. Jamain, J.H. Zaini, A.K. Azad, A review on proton conducting electrolytes for clean energy and intermediate temperature-solid oxide fuel cells, Renew. Sustain. Energy Rev. 79 (2017) 750–764, https://doi.org/10.1016/j.rser.2017.05.147.

[69] Y. Zhao, D. Weidner, Thermal expansion of $SrZrO_3$ and $BaZrO_3$ perovskites, Phys. Chem. Miner. 18 (1991) 38–79, https://doi.org/10.1007/BF00200187.

[70] D.W. Kang, K.A. Lee, M. Kang, J.M. Kim, M. Moon, J.H. Choe, H. Kim, D.W. Kim, J.Y. Kim, C.S. Hong, Cost-effective porous-organic-polymer-based electrolyte membranes with superprotonic conductivity and low activation energy, J. Mater. Chem. A. 8 (2020) 1147–1153, https://doi.org/10.1039/C9TA06807D.

[71] N. Kochetova, I. Animitsa, D. Medvedev, A. Demin, P. Tsiakaras, Recent activity in the development of proton-conducting oxides for high-temperature applications, RSC Adv. 6 (2016) 73222–73268, https://doi.org/10.1039/C6RA13347A.

[72] N. Fukatsu, N. Kurita, Proton conduction in α-alumina and its application to hydrogen sensor for molten metals, Ionics 13 (2007) 183–194, https://doi.org/10.1007/s11581-007-0092-0.

[73] Y. Meng, J. Gao, Z. Zhao, J. Amoroso, J. Tong, K.S. Brinkman, Review: recent progress in low-temperature proton-conducting ceramics, J. Mater. Sci. 54 (2019) 9291–9312, https://doi.org/10.1007/s10853-019-03559-9.

[74] T. Norby, Proton conductivity in perovskite oxides. https://doi.org/10.1007/978-0-387-77708-5_11, 2009, 217-241.

[75] A.B. Lavand, Y.S. Malghe, Synthesis of nanosized $BaZrO_3$ from oxalate precursor, J. Therm. Anal. Calorim. 118 (2014) 1613–1618, https://doi.org/10.1007/s10973-014-4033-7.

[76] A. Sin, B. Montaser, P. Odier, F. Weiss, Synthesis and sintering of large batches of barium zirconate nanopowders, J. Am. Ceram. Soc. 85 (2002) 1928–1932, https://doi.org/10.1111/j.1151-2916.2002.tb00382.x.

[77] A. Perrichon, E. Jedvik Granhed, G. Romanelli, A. Piovano, A. Lindman, P. Hyldgaard, G. Wahnström, M. Karlsson, Unraveling the ground-state structure of $BaZrO_3$ by neutron scattering experiments and first-principles calculations, Chem. Mater. 32 (2020) 2824–2835, https://doi.org/10.1021/acs.chemmater.9b04437.

[78] A.R. Akbarzadeh, I. Kornev, C. Malibert, L. Bellaiche, J.M. Kiat, Combined theoretical and experimental study of the low-temperature properties of $BaZrO_3$, Phys. Rev. B 72 (2005) 205104, https://doi.org/10.1103/PhysRevB.72.205104.

[79] M.D. McDaniel, T.Q. Ngo, S. Hu, A. Posadas, A.A. Demkov, J.G. Ekerdt, Atomic layer deposition of perovskite oxides and their epitaxial integration with Si, Ge, and other semiconductors, Appl. Phys. Rev. 2 (2015), 041301, https://doi.org/10.1063/1.4934574.

[80] M.K. Hossain, K. Hashizume, Y. Hatano, Evaluation of the hydrogen solubility and diffusivity in proton-conducting oxides by converting the PSL values of a tritium imaging plate, Nucl. Mater. Energy. 25 (2020) 100875, https://doi.org/10.1016/j.nme.2020.100875.

[81] F.J.A. Loureiro, N. Nasani, G.S. Reddy, N.R. Munirathnam, D.P. Fagg, A review on sintering technology of proton conducting $BaCeO_3$-$BaZrO_3$ perovskite oxide materials for Protonic Ceramic Fuel Cells, J. Power Sources 438 (2019) 226991, https://doi.org/10.1016/j.jpowsour.2019.226991.

[82] M.F. Shukur, M.F.Z. Kadir, Hydrogen ion conducting starch-chitosan blend based electrolyte for application in electrochemical devices, Electrochim. Acta 158 (2015) 152–165, https://doi.org/10.1016/j.electacta.2015.01.167.

[83] H. Gu, Z. Wang, Y. Hu, Hydrogen gas sensors based on semiconductor oxide nanostructures, Sensors 12 (2012) 5517–5550, https://doi.org/10.3390/s120505517.

[84] Y. Tong, Y. Wang, C. Cui, S. Wang, B. Xie, R. Peng, C. Chen, Z. Zhan, Preparation and characterization of symmetrical protonic ceramic fuel cells as electrochemical hydrogen pumps, J. Power Sources 457 (2020) 228036, https://doi.org/10.1016/j.jpowsour.2020.228036.

[85] O. Paschos, J. Kunze, U. Stimming, F. Maglia, A review on phosphate based, solid state, protonic conductors for intermediate temperature fuel cells, J. Phys. Condens. Matter 23 (2011) 234110, https://doi.org/10.1088/0953-8984/23/23/234110.

[86] A.J. Abd Aziz, N.A. Baharuddin, M.R. Somalu, A. Muchtar, Review of composite cathodes for intermediate-temperature solid oxide fuel cell applications, Ceram. Int. (2020), https://doi.org/10.1016/j.ceramint.2020.06.176.

[87] N.S. Patki, A. Manerbino, J.D. Way, S. Ricote, Galvanic hydrogen pumping performance of copper electrodes fabricated by electroless plating on a $BaZr_{0.9}Ce_{0.1}Y_{0.1}O_3$-proton-conducting ceramic membrane, Solid State Ionics 317 (2018) 256–262, https://doi.org/10.1016/j.ssi.2018.01.031.

[88] J. Choi, M. Shin, B. Kim, J.-S. Park, High-performance ceramic composite electrodes for electrochemical hydrogen pump using protonic ceramics, Int. J. Hydrogen Energy 42 (2017) 13092–13098, https://doi.org/10.1016/j.ijhydene.2017.04.061.

[89] S. Robinson, A. Manerbino, W. Grover Coors, Galvanic hydrogen pumping in the protonic ceramic perovskite, J. Membr. Sci. 446 (2013) 99–105, https://doi.org/10.1016/j.memsci.2013.06.026.

[90] D. Han, T. Uda, The best composition of an Y-doped $BaZrO_3$ electrolyte: selection criteria from transport properties, microstructure, and phase behavior, J. Mater. Chem. A. 6 (2018) 18571–18582, https://doi.org/10.1039/C8TA06280C.

[91] K. Bae, D.Y. Jang, H.J. Choi, D. Kim, J. Hong, B.-K. Kim, J.-H. Lee, J.-W. Son, J. H. Shim, Demonstrating the potential of yttrium-doped barium zirconate electrolyte for high-performance fuel cells, Nat. Commun. 8 (2017) 14553, https://doi.org/10.1038/ncomms14553.

[92] J. Bu, P.G. Jönsson, Z. Zhao, The effect of NiO on the conductivity of $BaZr_{0.5}Ce_{0.3}Y_{0.2}O_{3-\delta}$ based electrolytes, RSC Adv. 6 (2016) 62368–62377, https://doi.org/10.1039/C6RA09936J.

[93] D. Yun, J. Kim, S.-J. Kim, J.-H. Lee, J.-N. Kim, H. Yoon, J. Yu, M. Kwak, H. Yoon, Y. Cho, C.-Y. Yoo, Structural and electrochemical properties of dense yttria-doped barium zirconate prepared by solid-state reactive sintering, Energies 11 (2018) 3083, https://doi.org/10.3390/en11113083.

[94] S. Nikodemski, J. Tong, R. O'Hayre, Solid-state reactive sintering mechanism for proton conducting ceramics, Solid State Ionics 253 (2013) 201–210, https://doi.org/10.1016/j.ssi.2013.09.025.

[95] Z. Zhu, S. Wang, Investigation on samarium and yttrium co-doping barium zirconate proton conductors for protonic ceramic fuel cells, Ceram. Int. 45 (2019) 19289–19296, https://doi.org/10.1016/j.ceramint.2019.06.179.

[96] M. Irshad, Q. ul Ain, K. Siraj, R. Raza, A.N. Tabish, M. Rafique, R. Idrees, F. Khan, S. Majeed, M. Ahsan, Evaluation of $BaZr_{0.8}X_{0.2}$ (X= Y, Gd, Sm) proton conducting electrolytes sintered at low temperature for IT-SOFC synthesized by cost effective combustion method, J. Alloys Compd. 815 (2020) 152389, https://doi.org/10.1016/j.jallcom.2019.152389.

[97] S. Jeong, T. Kobayashi, K. Kuroda, H. Kwon, C. Zhu, H. Habazaki, Y. Aoki, Evaluation of thin film fuel cells with Zr-rich $BaZr_xCe_{0.8-x}Y_{0.2}O_{3-\delta}$ electrolytes ($x \geq 0.4$) fabricated by a single-step reactive sintering method, RSC Adv. 8 (2018) 26309–26317, https://doi.org/10.1039/C8RA04724C.

[98] D. Han, T. Uda, Correlation between phase behavior and electrical conductivity of 10 mol % Y-doped $BaZrO_3$: an anomalous dispersion effect-aided synchrotron radiation XRD study combined with TEM observation and electrochemical analysis, ACS Appl. Mater. Interfaces 11 (2019) 3990–4000, https://doi.org/10.1021/acsami.8b19576.

[99] M. Chen, D. Chen, K. Wang, Q. Xu, Densification and electrical conducting behavior of $BaZr_{0.9}Y_{0.1}O_{3-\delta}$ proton conducting ceramics with NiO additive, J. Alloys Compd. 781 (2019) 857–865, https://doi.org/10.1016/j.jallcom.2018.12.090.

[100] P. Hosseinabadi, K. Hooshyari, M. Javanbakht, M. Enhessari, Synthesis and optimization of nanocomposite membranes based on SPEEK and perovskite nanoparticles for polymer electrolyte membrane fuel cells, New J. Chem. 43 (2019) 16232–16245, https://doi.org/10.1039/C9NJ03980E.

[101] L. Rioja-Monllor, C. Bernuy-Lopez, M.-L. Fontaine, T. Grande, M.-A. Einarsrud, Processing of high performance composite cathodes for protonic ceramic fuel cells by exsolution, J. Mater. Chem. A. 7 (2019) 8609–8619, https://doi.org/10.1039/C8TA10950H.

[102] P. Seeharaj, T. Charoonsuk, P. Pasupong, P. Kim-Lohsoontorn, N. Vittayakorn, phase formation, microstructure, and densification of yttrium-doped barium zirconate prepared by the sonochemical method, Int. J. Appl. Ceram. Technol. 13 (2016) 200–208, https://doi.org/10.1111/ijac.12436.

[103] L. Bi, E.H. Da'as, S.P. Shafi, Proton-conducting solid oxide fuel cell (SOFC) with Y-doped $BaZrO_3$ electrolyte, Electrochem. Commun. 80 (2017) 20–23, https://doi.org/10.1016/j.elecom.2017.05.006.

[104] R. Sažinas, I. Sakaguchi, I. Hasle, J.M. Polfus, R. Haugsrud, M.-A. Einarsrud, T. Grande, Tracer diffusion of 96Zr and 134Ba in polycrystalline $BaZrO_3$, Phys. Chem. Chem. Phys. 19 (2017) 21878–21886, https://doi.org/10.1039/C7CP04039C.

[105] K. Hooshyari, S.N. Khanamiri, P. Salarizadeh, H. Beydaghi, Nanocomposite membranes with high fuel cell performance based on sulfonated poly (1,4-phenylene ether ether sulfone) and ytterbium/yttrium doped-perovskite nanoparticles, J. Electrochem. Soc. 166 (2019) F976–F989, https://doi.org/10.1149/2.1521912jes.

[106] A. Jarry, S. Ricote, A. Geller, C. Pellegrinelli, X. Zhang, D. Stewart, I. Takeuchi, E. Wachsman, E.J. Crumlin, B. Eichhorn, Assessing substitution effects on surface chemistry by in situ ambient pressure X-ray photoelectron spectroscopy on perovskite thin films, BaCe x Zr 0.9– x Y 0.1 O 2.95 (x = 0; 0.2; 0.9), ACS Appl. Mater. Interfaces 10 (2018) 37661–37670, https://doi.org/10.1021/acsami.8b12546.

[107] Z. Zhu, S. Wang, J. Shen, X. Meng, Y. Cao, Z. Wang, Z. Wei, Effect of low-level Ca^{2+} substitution at perovskite B site on the properties of $BaZr_{0.8}Y_{0.2}O_{3-\delta}$, J. Alloys Compd. 805 (2019) 718–724, https://doi.org/10.1016/j.jallcom.2019.07.128.

[108] J. Huang, Y. Ma, M. Cheng, S. Ruan, Fabrication of integrated BZY electrolyte matrices for protonic ceramic membrane fuel cells by tape-casting and solid-state reactive sintering, Int. J. Hydrogen Energy 43 (2018) 12835–12846, https://doi.org/10.1016/j.ijhydene.2018.04.148.

[109] A. Fluri, A. Marcolongo, V. Roddatis, A. Wokaun, D. Pergolesi, N. Marzari, T. Lippert, Enhanced proton conductivity in Y-doped $BaZrO_3$ via strain engineering, Adv. Sci. 4 (2017) 1700467, https://doi.org/10.1002/advs.201700467.

[110] G. Chen, Y. Luo, W. Sun, H. Liu, Y. Ding, Y. Li, S. Geng, K. Yu, G. Liu, Electrochemical performance of a new structured low temperature SOFC with BZY electrolyte, Int. J. Hydrogen Energy 43 (2018) 12765–12772, https://doi.org/10.1016/j.ijhydene.2018.04.006.

[111] M.D. Gonçalves, P.S. Maram, A. Navrotsky, R. Muccillo, Effect of synthesis atmosphere on the proton conductivity of Y-doped barium zirconate solid electrolytes, Ceram. Int. 42 (2016) 13689–13696, https://doi.org/10.1016/j.ceramint.2016.05.167.

[112] P. Babilo, S.M. Haile, Enhanced sintering of yttrium-doped barium zirconate by addition of ZnO, J. Am. Ceram. Soc. 88 (2005) 2362–2368, https://doi.org/10.1111/j.1551-2916.2005.00449.x.

[113] D. Noferini, B. Frick, M.M. Koza, M. Karlsson, Proton jump diffusion dynamics in hydrated barium zirconates studied by high-resolution neutron backscattering spectroscopy, J. Mater. Chem. A. 6 (2018) 7538–7546, https://doi.org/10.1039/C7TA10509F.

[114] P. Raiteri, J.D. Gale, G. Bussi, Reactive force field simulation of proton diffusion in $BaZrO_3$ using an empirical valence bond approach, J. Phys. Condens. Matter 23 (2011) 334213, https://doi.org/10.1088/0953-8984/23/33/334213.

[115] M.K. Hossain, H. Tamura, K. Hashizume, Visualization of hydrogen isotope distribution in yttrium and cobalt doped barium zirconates, J. Nucl. Mater. 538 (2020) 152207, https://doi.org/10.1016/j.jnucmat.2020.152207.

[116] Y. Wu, K. Li, Y. Yang, W. Song, Z. Ma, H. Chen, X. Ou, L. Zhao, M. Khan, Y. Ling, Investigation of Fe-substituted in $BaZr_{0.8}Y_{0.2}O_{3-\delta}$ proton conducting oxides as cathode materials for protonic ceramics fuel cells, J. Alloys Compd. 814 (2020) 152220, https://doi.org/10.1016/j.jallcom.2019.152220.

[117] D. Noferini, M.M. Koza, M. Karlsson, Localized proton motions in acceptor-doped barium zirconates, J. Phys. Chem. C 121 (2017) 7088–7093, https://doi.org/10.1021/acs.jpcc.7b00177.

[118] J. Ding, J. Balachandran, X. Sang, W. Guo, G.M. Veith, C.A. Bridges, C. M. Rouleau, J.D. Poplawsky, N. Bassiri-Gharb, P. Ganesh, R.R. Unocic, Influence of nonstoichiometry on proton conductivity in thin-film yttrium-doped barium zirconate, ACS Appl. Mater. Interfaces 10 (2018) 4816–4823, https://doi.org/10.1021/acsami.7b16900.

[119] D. Han, Y. Noda, T. Onishi, N. Hatada, M. Majima, T. Uda, Transport properties of acceptor-doped barium zirconate by electromotive force measurements, Int. J. Hydrogen Energy 41 (2016) 14897–14908, https://doi.org/10.1016/j.ijhydene.2016.07.036.

[120] S. Ricote, N. Bonanos, G. Caboche, Water vapour solubility and conductivity study of the proton conductor $BaCe_{(0.9-x)}Zr_xY_{0.1}O_{(3-\delta)}$, Solid State Ionics 180 (2009) 990–997, https://doi.org/10.1016/j.ssi.2009.03.016.

[121] T. Schober, Water vapor solubility and electrochemical characterization of the high temperature proton conductor $BaZr_{0.9}Y_{0.1}O_{2.95}$, Solid State Ionics 127 (2000) 351–360, https://doi.org/10.1016/S0167-2738(99)00283-0.

[122] C. Kjølseth, L.-Y. Wang, R. Haugsrud, T. Norby, Determination of the enthalpy of hydration of oxygen vacancies in Y-doped $BaZrO_3$ and $BaCeO_3$ by TG-DSC, Solid State Ionics 181 (2010) 1740–1745, https://doi.org/10.1016/j.ssi.2010.10.005.

[123] Y. Yamazaki, F. Blanc, Y. Okuyama, L. Buannic, J.C. Lucio-Vega, C.P. Grey, S. M. Haile, Proton trapping in yttrium-doped barium zirconate, Nat. Mater. 12 (2013) 647–651, https://doi.org/10.1038/nmat3638.

[124] A. Slodczyk, P. Colomban, S. Willemin, O. Lacroix, B. Sala, Indirect Raman identification of the proton insertion in the high-temperature [Ba/Sr][Zr/Ti]O_3 -modified perovskite protonic conductors, J. Raman Spectrosc. 40 (2009) 513–521, https://doi.org/10.1002/jrs.2157.

[125] C. Hiraiwa, D. Han, A. Kuramitsu, A. Kuwabara, H. Takeuchi, M. Majima, T. Uda, Chemical expansion and change in lattice constant of Y-doped $BaZrO_3$ by hydration/dehydration reaction and final heat-treating temperature, J. Am. Ceram. Soc. 96 (2013) 879–884, https://doi.org/10.1111/jace.12172.

[126] R. Sažinas, M.-A. Einarsrud, T. Grande, Toughening of Y-doped $BaZrO_3$ proton conducting electrolytes by hydration, J. Mater. Chem. A. 5 (2017) 5846–5857, https://doi.org/10.1039/C6TA11022C.

[127] G. Hudish, A. Manerbino, W.G. Coors, S. Ricote, Chemical expansion in $BaZr_{0.9-x}Ce_xY_{0.1}O_{3-\delta}$ (x = 0 and 0.2) upon hydration determined by high-temperature X-ray diffraction, J. Am. Ceram. Soc. 101 (2018) 1298–1309, https://doi.org/10.1111/jace.15275.

[128] Q. Chen, F. El Gabaly, F. Aksoy Akgul, Z. Liu, B.S. Mun, S. Yamaguchi, A. Braun, Observation of oxygen vacancy filling under water vapor in ceramic proton conductors in situ with ambient pressure XPS, Chem. Mater. 25 (2013) 4690–4696, https://doi.org/10.1021/cm401977p.

[129] Y. Ling, H. Chen, J. Niu, F. Wang, L. Zhao, X. Ou, T. Nakamura, K. Amezawa, Bismuth and indium co-doping strategy for developing stable and efficient barium zirconate-based proton conductors for high-performance H-SOFCs, J. Eur. Ceram. Soc. 36 (2016) 3423–3431, https://doi.org/10.1016/j.jeurceramsoc.2016.05.027.

[130] A. Satapathy, E. Sinha, B.K. Sonu, S.K. Rout, Conduction and relaxation phenomena in barium zirconate ceramic in wet N_2 environment, J. Alloys Compd. 811 (2019) 152042, https://doi.org/10.1016/j.jallcom.2019.152042.

[131] J. Xiao, H. Yuan, L. Chen, C. Xiong, J. Ma, Y. Zhao, J. Chai, W. Du, X. Zhu, Anode-supported $BaZr_{0.8}Y_{0.2}O_{3-\delta}$ membranes by tape casting and suspension spraying, Int. J. Mod. Phys. B 31 (2017) 1744062, https://doi.org/10.1142/S0217979217440623.

[132] H. Xie, Z. Wei, Y. Yang, H. Chen, X. Ou, B. Lin, Y. Ling, New Gd-Zn co-doping enhanced mechanical properties of $BaZrO_3$ proton conductors with high conductivity for IT-SOFCs, Mater. Sci. Eng. B 238–239 (2018) 76–82, https://doi.org/10.1016/j.mseb.2018.12.012.

[133] D. Yuansheng, X. Jinfeng, N. Hongqiang, Z. Guohong, J. Danyu, L. Qiang, Preparation and proton conductivity of ultrafine Y-doped $BaZrO_3$ ceramics, J. Ceram. Soc. Japan. 125 (2017) 520–523, https://doi.org/10.2109/jcersj2.17017.

[134] J. Jiao, Q. Li, Y. Gu, Y. Luo, L. Ge, Y. Zheng, H. Chen, L. Guo, Effect of BaO-B_2O_3 composite sintering aid on sinterability and electrical property of BaZr0.85Y0.15O3- ceramic, Ceram. Int. 45 (2019) 13679–13684, https://doi.org/10.1016/j.ceramint.2019.04.062.

[135] Y. Li, W. Yang, L. Wang, J. Zhu, W. Meng, Z. He, L. Dai, Improvement of sinterability of $BaZr_{0.8}Y_{0.2}O_{3-\delta}$ for H_2 separation using Li2O/ZnO dual-sintering aid, Ceram. Int. 44 (2018) 15935–15943, https://doi.org/10.1016/j.ceramint.2018.06.014.

[136] L. Ge, J. Jiao, Z. Zhu, Q. Zhang, Y. Zheng, H. Chen, L. Guo, A facile method to fabricate proton-conducting $BaZr_{0.85}Y_{0.15}O_3$- electrolyte with a large grain size

and high conductivity, Ceram. Int. 45 (2019) 24946–24952, https://doi.org/10.1016/j.ceramint.2019.08.202.
[137] H. Dai, Proton conducting solid oxide fuel cells with chemically stable $BaZr_{0.75}Y_{0.2}Pr_{0.05}O_{3-\delta}$ electrolyte, Ceram. Int. 43 (2017) 7362–7365, https://doi.org/10.1016/j.ceramint.2017.02.090.
[138] T. Kuroha, K. Yamauchi, Y. Mikami, Y. Tsuji, Y. Niina, M. Shudo, G. Sakai, N. Matsunaga, Y. Okuyama, Effect of added Ni on defect structure and proton transport properties of indium-doped barium zirconate, Int. J. Hydrogen Energy 45 (2020) 3123–3131, https://doi.org/10.1016/j.ijhydene.2019.11.128.
[139] S. Ricote, B.L. Kee, W.G. Coors, Channelized substrates made from $BaZr_{0.75}Ce_{0.05}Y_{0.2}O_{3-d}$ proton-conducting ceramic polymer clay, Membranes 9 (2019) 130, https://doi.org/10.3390/membranes9100130.
[140] J. Wallis, L. Urban, C. Grimmer, W. Bodnar, R. Zimmermann, S. Ricote, K.-D. Weltmann, E. Burkel, A. Kruth, Structural and electrical properties of $BaZr_{0.7}Ce_{0.2}Y_{0.1}O_{3-\delta}$ proton conducting ceramic fabricated by spark plasma sintering, Solid State Ionics 345 (2020) 115118, https://doi.org/10.1016/j.ssi.2019.115118.
[141] D. Han, K. Shinoda, S. Tsukimoto, H. Takeuchi, C. Hiraiwa, M. Majima, T. Uda, Origins of structural and electrochemical influence on Y-doped $BaZrO_3$ heat-treated with NiO additive, J. Mater. Chem. A. 2 (2014) 12552, https://doi.org/10.1039/C4TA01689K.
[142] W. Sun, Z. Zhu, Z. Shi, W. Liu, Chemically stable and easily sintered high-temperature proton conductor $BaZr_{0.8}In_{0.2}O_{3-\delta}$ for solid oxide fuel cells, J. Power Sources 229 (2013) 95–101, https://doi.org/10.1016/j.jpowsour.2012.12.017.
[143] W. Sun, Z. Shi, M. Liu, L. Bi, W. Liu, An easily sintered, chemically stable, barium zirconate-based proton conductor for high-performance proton-conducting solid oxide fuel cells, Adv. Funct. Mater. 24 (2014) 5695–5702, https://doi.org/10.1002/adfm.201401478.
[144] Y. Wen, S. Yang, S. Gu, X. Ye, Z. Wen, Fabrication and characterization of a double-layer electrolyte membrane for $BaCeO_3$ -based reversible solid oxide cells (RSOCs), Solid State Ionics 308 (2017) 167–172, https://doi.org/10.1016/j.ssi.2017.06.011.
[145] A. Dubois, S. Ricote, R.J. Braun, Benchmarking the expected stack manufacturing cost of next generation, intermediate-temperature protonic ceramic fuel cells with solid oxide fuel cell technology, J. Power Sources 369 (2017) 65–77, https://doi.org/10.1016/j.jpowsour.2017.09.024.
[146] E. Fabbri, L. Bi, H. Tanaka, D. Pergolesi, E. Traversa, Chemically stable Pr and Y Co-doped barium zirconate electrolytes with high proton conductivity for intermediate-temperature solid oxide fuel cells, Adv. Funct. Mater. 21 (2011) 158–166, https://doi.org/10.1002/adfm.201001540.
[147] I. Luisetto, S. Licoccia, A. D'Epifanio, A. Sanson, E. Mercadelli, E. Di Bartolomeo, Electrochemical performance of spin coated dense $BaZr_{0.80}Y_{0.16}Zn_{0.04}O_{3-\delta}$ membranes, J. Power Sources 220 (2012) 280–285, https://doi.org/10.1016/j.jpowsour.2012.07.136.
[148] Y. Liu, Y. Guo, R. Ran, Z. Shao, A new neodymium-doped $BaZr_{0.8}Y_{0.2}O_{3-\delta}$ as potential electrolyte for proton-conducting solid oxide fuel cells, J. Membr. Sci. 415–416 (2012) 391–398, https://doi.org/10.1016/j.memsci.2012.05.062.
[149] Y. Li, L.M. Wong, H. Xie, S. Wang, P.-C. Su, Nanoporous palladium anode for direct ethanol solid oxide fuel cells with nanoscale proton-conducting ceramic electrolyte, J. Power Sources 340 (2017) 98–103, https://doi.org/10.1016/j.jpowsour.2016.11.064.
[150] L. Bi, E. Fabbri, E. Traversa, Solid oxide fuel cells with proton-conducting $La_{0.99}Ca_{0.01}NbO_4$ electrolyte, Electrochim. Acta 260 (2018) 748–754, https://doi.org/10.1016/j.electacta.2017.12.030.
[151] Y. Li, S. Wang, P.-C. Su, Proton-conducting micro-solid oxide fuel cells with improved cathode reactions by a nanoscale thin film gadolinium-doped ceria interlayer, Sci. Rep. 6 (2016) 22369, https://doi.org/10.1038/srep22369.
[152] D. Han, A. Kuramitsu, T. Onishi, Y. Noda, M. Majima, T. Uda, Fabrication of protonic ceramic fuel cells via infiltration with Ni nanoparticles: a new strategy to suppress NiO diffusion & increase open circuit voltage, Solid State Ionics 345 (2020) 115189.
[153] L. Lei, Z. Tao, T. Hong, X. Wang, F. Chen, A highly active hybrid catalyst modified $(La_{0.60}Sr_{0.40})_{0.95}Co_{0.20}Fe_{0.80}O_{3-\delta}$ cathode for proton conducting solid oxide fuel cells, J. Power Sources 389 (2018) 1–7, https://doi.org/10.1016/j.jpowsour.2018.03.058.
[154] L. Bi, S.P. Shafi, E.H. Da'as, E. Traversa, Tailoring the cathode-electrolyte interface with nanoparticles for boosting the solid oxide fuel cell performance of chemically stable proton-conducting electrolytes, Small 14 (2018) 1801231, https://doi.org/10.1002/smll.201801231.
[155] E.H. Da'as, L. Bi, S. Boulfrad, E. Traversa, Nanostructuring the electronic conducting $La_{0.8}Sr_{0.2}MnO_{3-\delta}$ cathode for high-performance in proton-conducting solid oxide fuel cells below 600°C, Sci. China Mater. 61 (2018) 57–64, https://doi.org/10.1007/s40843-017-9125-1.
[156] L.P. Wendler, K. Ramos, D.M.P.F. Souza, Investigation about the reason of limited grain growth of Y-doped barium zirconate, Ceram. Int. 45 (2019) 19120–19126, https://doi.org/10.1016/j.ceramint.2019.06.158.
[157] Y. Yamazaki, R. Hernandez-Sanchez, S.M. Haile, Cation non-stoichiometry in yttrium-doped barium zirconate: phase behavior, microstructure, and proton conductivity, J. Mater. Chem. 20 (2010) 8158, https://doi.org/10.1039/c0jm02013c.
[158] S. Bhaskar Reddy, K. Prasad Rao, M.S. Ramachandra Rao, Influence of A-site Gd doping on the microstructure and dielectric properties of $Ba(Zr_{0.1}Ti_{0.9})O_3$ ceramics, J. Alloys Compd. 509 (2011) 1266–1270, https://doi.org/10.1016/j.jallcom.2010.09.211.
[159] D. Han, Y. Nose, K. Shinoda, T. Uda, Site selectivity of dopants in $BaZr_{1-y}MyO_{3-\delta}$ (M = Sc, Y, Sm, Eu, Dy) and measurement of their water contents and conductivities, Solid State Ionics 213 (2012) 2–7, https://doi.org/10.1016/j.ssi.2011.09.005.
[160] E. Makagon, R. Merkle, J. Maier, I. Lubomirsky, Influence of hydration and dopant ionic radius on the elastic properties of $BaZrO_3$, Solid State Ionics 344 (2020) 115130, https://doi.org/10.1016/j.ssi.2019.115130.
[161] D. Medvedev, A. Murashkina, E. Pikalova, A. Demin, A. Podias, P. Tsiakaras, $BaCeO_3$: materials development, properties and application, Prog. Mater. Sci. 60 (2014) 72–129, https://doi.org/10.1016/j.pmatsci.2013.08.001.
[162] F. Yang, H. Zhang, L. Li, I.M. Reaney, D.C. Sinclair, High ionic conductivity with low degradation in A-site strontium-doped nonstoichiometric sodium bismuth titanate perovskite, Chem. Mater. 28 (2016) 5269–5273, https://doi.org/10.1021/acs.chemmater.6b02555.
[163] C. Zhang, H. Zhao, A novel cobalt-free cathode material for proton-conducting solid oxide fuel cells, J. Mater. Chem. 22 (2012) 18387, https://doi.org/10.1039/c2jm32627b.
[164] Z. Tao, L. Bi, Z. Zhu, W. Liu, Novel cobalt-free cathode materials $BaCexFe_{1-x}O_{3-\delta}$ for proton-conducting solid oxide fuel cells, J. Power Sources 194 (2009) 801–804, https://doi.org/10.1016/j.jpowsour.2009.06.071.
[165] P. Babilo, T. Uda, S.M. Haile, Processing of yttrium-doped barium zirconate for high proton conductivity, J. Mater. Res. 22 (2007) 1322–1330, https://doi.org/10.1557/jmr.2007.0163.
[166] R. Muccillo, E.N.S. Muccillo, T.F. Andrade, O.R. Oliveira, Thermal analyses of yttrium-doped barium zirconate with phosphor pentoxide, boron oxide and zinc oxide addition, J. Therm. Anal. Calorim. 130 (2017) 1791–1799, https://doi.org/10.1007/s10973-017-6523-x.
[167] K.-Y. Park, Y. Seo, K.B. Kim, S.-J. Song, B. Park, J.-Y. Park, Enhanced proton conductivity of yttrium-doped barium zirconate with sinterability in protonic ceramic fuel cells, J. Alloys Compd. 639 (2015) 435–444, https://doi.org/10.1016/j.jallcom.2015.03.168.
[168] S. Tao, J.T.S. Irvine, Conductivity studies of dense yttrium-doped $BaZrO_3$ sintered at 1325°C, J. Solid State Chem. 180 (2007) 3493–3503, https://doi.org/10.1016/j.jssc.2007.09.027.
[169] M. Biswas, H. An, S.M. Choi, J.-W. Son, J.-H. Lee, B.-K. Kim, H.-W. Lee, K.J. Yoon, Low-temperature sintering of $Ba(Zr,Y)O_3$ -based proton conducting oxides using BaO–CuO eutectic flux as sintering aid, Ceram. Int. 42 (2016) 10476–10481, https://doi.org/10.1016/j.ceramint.2016.03.038.
[170] S. Duval, P. Holtappels, U. Vogt, E. Pomjakushina, K. Conder, U. Stimming, T. Graule, Electrical conductivity of the proton conductor $BaZr_{0.9}Y_{0.1}O_{3-\delta}$ obtained by high temperature annealing, Solid State Ionics 178 (2007) 1437–1441, https://doi.org/10.1016/j.ssi.2007.08.006.
[171] J.M. Serra, W.A. Meulenberg, Thin-film proton $BaZr_{0.85}Y_{0.15}O_3$ conducting electrolytes: toward an intermediate-temperature solid oxide fuel cell alternative, J. Am. Ceram. Soc. 90 (2007) 2082–2089, https://doi.org/10.1111/j.1551-2916.2007.01677.x.
[172] E. Fabbri, D. Pergolesi, E. Traversa, Materials challenges toward proton-conducting oxide fuel cells: a critical review, Chem. Soc. Rev. 39 (2010) 4355, https://doi.org/10.1039/b902343g.
[173] J.M. Polfus, T.S. Bjørheim, T. Norby, R. Bredesen, Surface defect chemistry of Y-substituted and hydrated $BaZrO_3$ with subsurface space-charge regions, J. Mater. Chem. A. 4 (2016) 7437–7444, https://doi.org/10.1039/C6TA02067D.
[174] D. Han, S. Uemura, C. Hiraiwa, M. Majima, T. Uda, Detrimental effect of sintering additives on conducting ceramics: yttrium-doped barium zirconate, ChemSusChem 11 (2018) 4102–4113, https://doi.org/10.1002/cssc.201801837.
[175] D. Han, L. Jiang, P. Zhong, Improving phase compatibility between doped $BaZrO_3$ and NiO in protonic ceramic cells via tuning composition and dopant, Int. J. Hydrogen Energy 46 (2021) 8767–8777, https://doi.org/10.1016/j.ijhydene.2020.12.075.
[176] D. Han, K. Shinoda, S. Sato, M. Majima, T. Uda, Correlation between electroconductive and structural properties of proton conductive acceptor-doped barium zirconate, J. Mater. Chem. A. 3 (2015) 1243–1250, https://doi.org/10.1039/C4TA05701E.
[177] E. Fabbri, A. Depifanio, E. Dibartolomeo, S. Licoccia, E. Traversa, Tailoring the chemical stability of $Ba(Ce_{0.8-x}Zr_x)Y_{0.2}O_{3-\delta}$ protonic conductors for intermediate temperature solid oxide fuel cells (IT-SOFCs), Solid State Ionics 179 (2008) 558–564, https://doi.org/10.1016/j.ssi.2008.04.002.
[178] K.D. Kreuer, Aspects of the formation and mobility of protonic charge carriers and the stability of perovskite-type oxides, Solid State Ionics 125 (1999) 285–302, https://doi.org/10.1016/S0167-2738(99)00188-5.
[179] D. Pergolesi, E. Fabbri, A. D'Epifanio, E. Di Bartolomeo, A. Tebano, S. Sanna, S. Licoccia, G. Balestrino, E. Traversa, High proton conduction in grain-boundary-free yttrium-doped barium zirconate films grown by pulsed laser deposition, Nat. Mater. 9 (2010) 846–852, https://doi.org/10.1038/nmat2837.
[180] J. Exner, T. Nazarenus, J. Kita, R. Moos, Dense Y-doped ion conducting perovskite films of $BaZrO_3$, $BaSnO_3$, and $BaCeO_3$ for SOFC applications produced by powder aerosol deposition at room temperature, Int. J. Hydrogen Energy 45 (2020) 10000–10016, https://doi.org/10.1016/j.ijhydene.2020.01.164.
[181] H. Zhang, B.A. Wilhite, Electrical conduction and hydrogen permeation investigation on iron-doped barium zirconate membrane, J. Membr. Sci. 512 (2016) 104–110, https://doi.org/10.1016/j.memsci.2016.04.001.
[182] X. Meng, Y. Shang, B. Meng, N. Yang, X. Tan, J. Sunarso, S. Liu, Bi-functional performances of $BaCe_{0.95}Tb_{0.05}O_{3-\delta}$-based hollow fiber membranes for power generation and hydrogen permeation, J. Eur. Ceram. Soc. 36 (2016) 4123–4129, https://doi.org/10.1016/j.jeurceramsoc.2016.06.041.
[183] M. Zhang, J. Xu, G. Ma, Proton conduction in $BaxCe_{0.8}Y_{0.2}O_{3-\alpha}$ + 0.04ZnO at intermediate temperatures and its application in ammonia synthesis at

atmospheric pressure, J. Mater. Sci. 46 (2011) 4690–4694, https://doi.org/10.1007/s10853-011-5376-0.

[184] S. Klinsrisuk, J.T.S. Irvine, Electrocatalytic ammonia synthesis via a proton conducting oxide cell with $BaCe_{0.5}Zr_{0.3}Y_{0.16}Zn_{0.04}O_3$-Δ electrolyte membrane, Catal. Today 286 (2017) 41–50, https://doi.org/10.1016/j.cattod.2016.06.051.

[185] E. Vasileiou, V. Kyriakou, I. Garagounis, A. Vourros, A. Manerbino, W.G. Coors, M. Stoukides, Electrochemical enhancement of ammonia synthesis in a $BaZr_{0.7}Ce_{0.2}Y_{0.1}O_{2.9}$ solid electrolyte cell, Solid State Ionics 288 (2016) 357–362, https://doi.org/10.1016/j.ssi.2015.12.022.

[186] H. Matsumoto, Y. Kawasaki, N. Ito, M. Enoki, T. Ishihara, Relation between electrical conductivity and chemical stability of $BaCeO_3$-based proton conductors with different trivalent dopants, Electrochem. Solid State Lett. 10 (2007), https://doi.org/10.1149/1.2458743.

[187] J. Lü, L. Wang, L. Fan, Y. Li, L. Dai, H. Guo, Chemical stability of doped $BaCeO_3$-$BaZrO_3$ solid solutions in different atmospheres, J. Rare Earths 26 (2008) 505–510, https://doi.org/10.1016/S1002-0721(08)60127-1.